MBoC | ARTICLE

Ninein promotes F-actin cup formation and inward phagosome movement during phagocytosis in macrophages

Safia Omer[a], Jiahao Li[b], Claire X. Yang[a], and Rene E. Harrison[a,b,*]
[a]Department of Biological Sciences, and [b]Department of Cell & Systems Biology, University of Toronto Scarborough, Toronto, Ontario M1C 1A4

ABSTRACT **Phagocytosis by macrophages is a highly polarized process to destroy large target cells. Binding to particles induces extensive cortical actin-generated forces that drive the formation of elaborate pseudopods around the target particle. Postinternalization, the resultant phagosome is driven toward the cell interior on microtubules (MTs) by cytoplasmic dynein. However, it is unclear whether dynein and cargo-adaptors contribute to the earlier steps of particle internalization and phagosome formation. Here we reveal that ninein, a MT minus-end-associated protein that localizes to the centrosome, is also present at the phagocytic cup in macrophages. Ninein depletion impairs particle internalization by delaying the early F-actin recruitment to sites of particle engagement and cup formation, with no impact on F-actin dynamics beyond this initial step. Ninein forms membrane-bound clusters on phagocytic cups that do not nucleate acentrosomal MTs but instead mediate the assembly of dynein–dynactin complex at active phagocytic membranes. Both ninein depletion and pharmacological inhibition of dynein activity reduced inward displacement of bound particles into macrophages. We found that ninein and dynein motor activity were required for timely retrograde movement of phagosomes and for phagolysosome formation. Taken together, these data show that ninein, alone and with dynein, play significant roles during phagocytosis.**

SIGNIFICANCE STATEMENT

- Phagocytosis by macrophages is driven extensively by F-actin forces that generate membrane pseudopods around target particles. However, the contribution of microtubule (MT) and associated proteins in these initial phagocytosis steps is unclear.
- In macrophages, the authors used siRNA depletion strategies to show a requirement for the dynein adaptor ninein for the initial the recruitment of F-actin at sites of bound particles.
- Additionally, ninein presence was important to cluster dynein–dynactin complexes at the phagocytic cup where motor action mediated early phagosome translocation into macrophages. These findings support the significance of MT-associated proteins and motors in generating a robust immune response.

Monitoring Editor
Sergio Grinstein
Hospital for Sick Children

Received: Jun 12, 2023
Revised: Nov 30, 2023
Accepted: Dec 12, 2023

This article was published online ahead of print in MBoC in Press (http://www.molbiolcell.org/cgi/doi/10.1091/mbc.E23-06-0216) on December 20, 2023.

*Address correspondence to: Rene E. Harrison (rene.harrison@utoronto.ca).

INTRODUCTION

Cytoplasmic dynein is an ATP-driven motor complex that plays a critical role in many specialized cells including immune cells. For instance, within minutes of T-cell activation, dynein coordinates the translocation of the microtubule-organizing center (MTOC) toward the T cell-antigen presenting cell interface (Combs *et al.*, 2006; Martín-Cófreces *et al.*, 2008; Yi *et al.*, 2013). In phagocytic macrophages, dynein activity is thought to coincide with its clustering in cholesterol-rich

microdomains on the surface of late phagosomes (Rai *et al.*, 2016). Dynein and its cofactor dynactin associate with late phagosomes (Blocker *et al.*, 1997; Habermann *et al.*, 2001) with the cargo adaptor RILP, to drive phagosome movement on MT tracks toward the MTOC (Blocker *et al.*, 1997; Harrison *et al.*, 2003). This recruitment of dynein is key for phagosome-lysosome fusion (Harrison and Grinstein, 2002; Harrison *et al.*, 2003), a process required for pathogen degradation and antigen presentation (Levin *et al.*, 2016). Little is known about how and when dynein is recruited to the surface of phagosomes to power retrograde trafficking. Dynein recruitment and activity is highly regulated by dynactin (Waterman-storer *et al.*, 1997; Schroer, 2004) and several families of coiled-coil cargo adaptor proteins that stabilize dynein–dynactin interactions, activate dynein motility, and participate in cargo selectivity (Urnavicius *et al.*, 2015; Reck-Peterson *et al.*, 2018; Olenick and Holzbaur, 2019).

In many cell types, the dynein adaptor ninein, localizes to the distal appendages surrounding the mother centriole interacting with γ-tubulin that nucleate MT arrays (Bouckson-Castaing *et al.*, 1996; Mogensen *et al.*, 2000; Piel *et al.*, 2000; Delgehyr *et al.*, 2005). In several polarized cells such as neurons, polarized MDCKII cells, and cochlear epithelial inner and outer pillar cells, ninein translocates from the centrosome to the cell cortex to form noncentrosomal MTOCs (Mogensen *et al.*, 2000; Moss *et al.*, 2007; Goldspink *et al.*, 2017; He *et al.*, 2022), playing an important role in MT organization at these sites. Like other dynein adaptors, ninein contains several coiled coil domains (Bouckson-Castaing *et al.*, 1996) and coimmunoprecipitates with dynein and dynactin (Casenghi *et al.*, 2005; Redwine *et al.*, 2017). Ninein activates dynein–dynactin processive movement in single-molecule motility assays in vitro (Redwine *et al.*, 2017) and overexpression of the N-terminus of ninein causes Golgi fragmentation (Casenghi *et al.*, 2005). However, in vivo evidence showing a role for ninein in dynein activity regulation, is still lacking.

Engulfment and internalization of particles into the cytoplasm of macrophages requires substantial cytoskeletal forces (Jaumouillé and Waterman, 2020; Vorselen *et al.*, 2020a). Fcγ receptor (FcγR) engagement with IgG-coated targets triggers a cascade of signaling events leading to a local burst of F-actin polymerization to physically deform the plasma membrane into a phagocytic cup (Castellano *et al.*, 2001; Campellone and Welch, 2010; Rougerie *et al.*, 2013; Levin *et al.*, 2015). The elaboration of the membrane pseudopods around the target particle is generated by F-actin protrusive forces and several F-actin motors, namely myosin I (MyoIg, MyoIe, and MyoIf) and myosin II (Swanson *et al.*, 1999; Kovari *et al.*, 2016). Myosin I isoforms localize to the extending cup on podosome-like structures containing Arp2/3-mediated F-actin enrichments (Barger *et al.*, 2019; Vorselen *et al.*, 2021). Myosin II operates later and forms contractile rings required for proper localization of the F-actin ring within and at the rim of the cup (Vorselen *et al.*, 2021). The resultant actomyosin activities power productive actin polymerization that drives membrane extension at the leading edge of the cup as well as target constriction (Araki *et al.*, 2003; Vorselen *et al.*, 2021) and phagosome closure (Swanson *et al.*, 1999; Kovari *et al.*, 2016; Barger *et al.*, 2019; Vorselen *et al.*, 2021) which coincides with actin disassembly at the base of the phagosome (Swanson *et al.*, 1999; Scott *et al.*, 2005). Once the particle is internalized, dynein-dependent retrograde trafficking of the phagosome is antagonized by the activity of myosin-Va, which delays the phagosomes from docking at the plus-end of MTs following phagosome internalization (Al-Haddad *et al.*, 2001). This data suggests that dynein activity is not contributing to earlier stages of engulfment but is rather restricted to the long-range retrograde trafficking of maturing phagosomes. Here, we revisited this notion, and examined the role of dynein and its adaptor ninein during particle binding and nascent phagosome formation and inward translocation in macrophages.

Using live cell imaging and immunostaining analysis of ninein depleted cells, we showed that ninein is required for the early stages of F-actin polymerization in pseudopods postbinding to IgG-bound targets, that subsequently promote the timely formation of the phagocytic cup, and particle internalization. Furthermore, we revealed that ninein forms distinct cortical clusters distributed to the side and the base of the phagocytic cup that specifically recruit dynein–dynactin clusters. Experimental downregulation of ninein protein levels or dynein motor activity stalled the inward displacement of forming phagosomes, and slowed phagosome movement. This reduced inward movement occurred despite the intact F-actin dynamics that is required for internalization. We showed that both ninein depletion and inhibiting dynein motility has downstream effects on phagolysosome formation.

RESULTS

Ninein accumulates at the phagocytic cup membrane

The capacity for ninein to bind and activate dynein motility in vitro (Redwine *et al.*, 2017) made us wonder if this adaptor plays a role in phagocytosis in macrophages. First, we examined ninein cellular localization in macrophages using immunofluorescence and confocal imaging of resting RAW 264.7 (RAW) cells (Figure 1A). In unstimulated macrophages, ninein was enriched at the perinuclear MTOC and formed speckles throughout the cytosol, with no visible detection at the plasma membrane (Figure 1B). Similar localization of ninein at centrosomes has been reported in other cell types (Bouckson-Castaing *et al.*, 1996; Chen *et al.*, 2003; Baird *et al.*, 2004; Delgehyr *et al.*, 2005; Lin *et al.*, 2006; Moss *et al.*, 2007; Ohama and Hayashi, 2009; Lecland *et al.*, 2019). We next examined ninein cellular localization during FcγR-mediated phagocytosis. Using classic phagocytosis assays (Figure 1C), RAW cells were challenged with IgG-opsonized sheep RBCs (IgG-sRBCs) for 7 min before fixing cells and immunostaining for ninein. Ninein signal was strong at the site of bound IgG-sRBCs (Figure 1D). We also examined ninein recruitment to protracted pseudopods that develop during frustrated phagocytosis (Masters *et al.*, 2013; Kovari *et al.*, 2016). Frustrated phagocytosis assays induce macrophages to form planar pseudopod extensions via rapid F-actin-mediated cell spreading over IgG-coated coverslips (Figure 1E). Interestingly, immunostaining analysis of ninein in macrophages after 10 min of frustrated phagocytosis showed accumulation of endogenous ninein at the cell – substrate interface at the frustrated phagocytic cup, which strongly colocalized with enriched F-actin (Figure 1F). To gain insight into the three-dimensional distribution of ninein during particle engulfment we examined ninein localization using a modified frustrated phagocytosis assay (Marie-Anaïs *et al.*, 2016; Mularski *et al.*, 2018), where cells are seeded on coverslips coated with noncovalently attached IgG-sRBCs, hence allowing cup formation and phagosome membrane extension around the particle but not engulfment, resulting in incomplete phagocytosis (Figure 1G). Rendering Z-stack of confocal images into montages showed ninein as discrete clusters with high intensity that are uniformly distributed along the sides and base of phagosome membranes around IgG-particles and at the site of phagosome closure (Figure 1H). Measuring the intensity profile through individual particles showed a clear enhancement of ninein around IgG-sRBCs (Figure 1I). Collectively, our data show that ninein is present as clusters at the phagocytic membrane before particle internalization in FcγR-mediated phagocytosis.

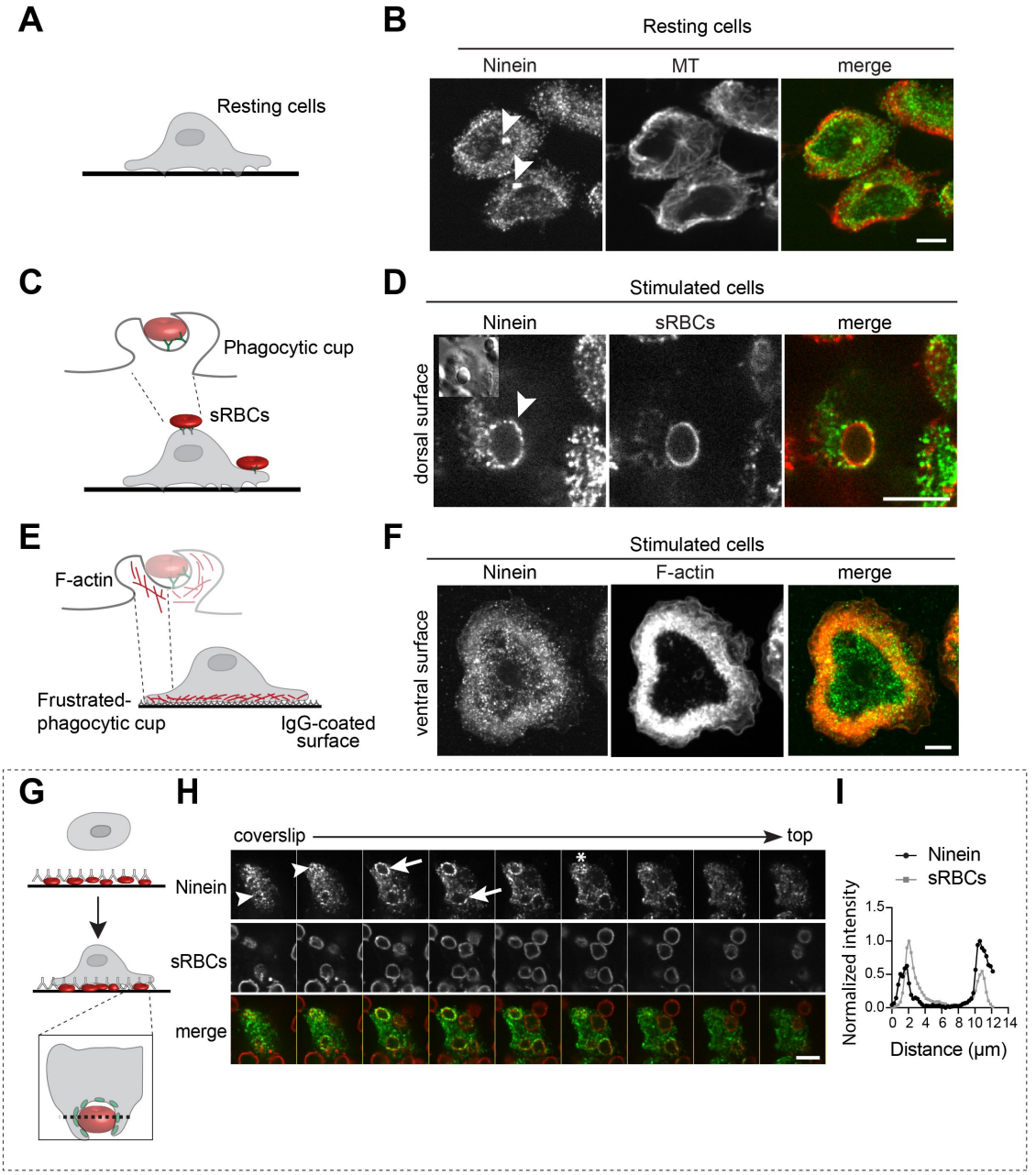

FIGURE 1: Ninein localizes to phagocytic cups in macrophages. (A) Diagram of resting Raw264.7 (RAW) cells cultured on coverslips. (B) Ninein localization in resting RAW cells fixed and immunostained for α-tubulin (MT; *red*) and ninein (*green*). Arrowheads indicate ninein enrichment at the MTOC. (C) Diagram of phagocytic assay where macrophages are given IgG-sRBCs. (D) Confocal images showing ninein localization around IgG-sRBCs in RAW cells stimulated for 7 min with sRBCs and immunostained for ninein. Inset shows a DIC image of IgG-sRBCs in contact with the surface of a RAW cell. (E) Diagram of macrophage undergoing frustrated phagocytosis on IgG-coated coverslips. The pseudopod extends across the opsonized coverslip, forming a structure equivalent to the conventional phagocytic cup (Masters *et al.*, 2013). (F) Confocal images showing ninein and F-actin localization at the frustrated phagocytic cup in RAW cells plated on IgG-coated coverslips for 10 min. (G) Diagram of a modified frustrated phagocytosis assay (Mularski *et al.*, 2018) where RAW cells were plated on immobilized IgG-particles to generate incomplete phagocytic events. Dashed line indicates site of intensity profile analysis in Figure 1I. (H) RAW cells were cultured for 10 min on immobilized IgG-sRBCs before being fixed and immunostained for ninein and sRBCs. Confocal Z-stack montage of a RAW cell showing ninein foci on pseudopod membranes (arrow), closure sites (arrowhead), and at the base of the cup (asterisk). (I) Representative example of normalized intensity profile of ninein signal along the line across the phagocytic membrane surrounding IgG-sRBCs. Scale bars = 10 μm.

Ninein is required for efficient phagocytosis

We next assessed whether ninein is required for phagocytosis by reducing protein levels with ninein SMARTpool siRNA and comparing particle uptake with cells treated with nontargeting control SMARTpool siRNA. The reduction in expression of endogenous ninein protein levels in siRNA-treated cells was first confirmed using

western blotting (Figure 2A) and immunostaining (Figure 2B). To determine whether phagocytosis was affected by ninein depletion we synchronized phagocytosis through a pulse-chase protocol. RAW cells were first treated with ninein-targeting or control siRNA and then challenged with IgG-beads for a 7-min pulse, followed by a wash to remove unbound particles and a 10-min chase. These time frames enabled us to capture the early defects during phagocytic cup formation and closure. Ninein-depleted cells had a significantly lower phagocytic index, compared with cells treated with control siRNA (Figure 2, B and C). To examine whether a particle binding defect could account for the reduced phagocytic activity, we assessed the binding of IgG-targets to the macrophage surface by challenging cells with IgG-beads for 7 min. Binding index quantification showed that ninein-depleted cells bound a similar number of 3.9 μm IgG-beads, compared with control cells (Figure 2D), suggesting that ninein is not required for target capture. Similar results were also obtained upon examining binding index of cells challenged with IgG-sRBCs for 4 min (1.23 ± 0.25 for ninein-depleted cells vs. 1 in control; normalized mean ± SD, $n \geq 368$, from three experiments). Next, we assessed the particle internalization efficiency, which is marked by phagosome closure, by distinguishing engulfed beads from fluorescently labeled bound beads that were stained before cell permeabilization. We observed fewer number of ninein-depleted cells containing internalized beads compared with control cells (Figure 2E). We also quantified the percentage of internalized beads relative to total number of beads (number of internalized beads/ sum of bound and internalized beads) and found a significant decrease in the percentage of internalized IgG-beads in ninein-depleted cells compared with control cells (Figure 2F). Furthermore, a smaller percentage of ninein-depleted cells were able to engulf ≥ three IgG-beads, compared with control cells (Figure 2G). We next investigated whether depletion of ninein inhibits or delays particle internalization. Control and ninein-depleted cells were exposed to 6.92 μm IgG-coated beads, followed by a washing step to remove unbound particles. Cells were then incubated in siRNA-containing medium for chase periods of 12, 30, and 60 min. In cells with reduced ninein, longer chase periods (30 and 60 min) significantly improved uptake compared with a 12-min incubation (Figure 2, H and I). Furthermore, we observed that ninein-depleted cells showed similar particle internalization to control cells after a 60-min incubation (Figure 2, H and I). Collectively, our results show that ninein depletion does not impact engagement with targets but delays particle internalization.

Ninein depletion delays initial F-actin recruitment to sites of bound particles

Next, we sought to determine the mechanism underling the defective particle internalization in ninein-depleted cells by examining the early steps of phagocytic cup formation (Figure 3A). To track F-actin dynamics on the phagocytic membrane, we performed live cell imaging of RAW cells stably expressing the fluorescent LifeAct construct (LifeAct-RFP). Cells were treated with ninein-targeting siRNA or nontargeting control siRNA and then exposed to IgG-sRBCs. To prevent including events of nonspecific binding of sRBCs to macrophages during live cell imaging, we analyzed F-actin dynamics exclusively in particles that were successfully internalized. As expected, in control cells, we observed a robust enrichment of F-actin fluorescence signal at the particle/ cell membrane interface following firm contact with IgG-sRBCs (Figure 3B). In contrast, we found that ninein-depleted cells showed a longer time before a detectable LifeAct-RFP signal was observed following binding (Figure 3B). Image analysis and quantification of the interval between binding of IgG-sRBCs and the appearance of LifeAct fluorescence signal at attachment sites showed significant longer intervals in ninein-depleted cells compared with control cells (88.76 s ± 16.75 s compared with 40.12 s ± 8.43 s in control cells, respectively; Figure 3C). To confirm this observation, we challenged ninein-depleted cells with IgG-sRBCs for 4 min before cells were fixed, immunostained for ninein and actin to detect endogenous proteins. In the absence of ninein, a smaller percentage of bound particles were able to elicit F-actin recruitment at the site of contact compared with IgG-sRBCs particles in control cells (31.03 ± 3.24% vs. 48.53 ± 2.70%, respectively; Mean ± SEM; $n \geq 203$; $p < 0.0001$ from three experiments), further supporting the role of ninein in promoting the early recruitment of F-actin to the site of bound particles in macrophages.

To test whether ninein is required for F-actin cup formation beyond the stalled initial F-actin recruitment, we examined F-actin temporal dynamics during F-actin ring formation (time between initial F-actin polymerization at the cell surface to formation of a complete F-actin ring around the particle) and F-actin ring duration (time between F-actin ring formation to F-actin disappearance from the nascent phagosome). Image analysis revealed that both F-actin temporal elements were similar during phagocytosis in ninein-depleted cells compared with control cells (Figure 3, D and E). Next, we measured LifeAct-RFP intensity over the entire duration of phagocytic events in live cells using confocal microscope imaging. As depletion of ninein induces significant delay in F-actin recruitment postbinding (Figure 3, B and C), we adjusted the tracking of actin intensities to start at the initial recruitment of F-actin at the contact site ($t = 0$), over time until the F-actin signal subsided from the phagosome. We found that ninein-depleted cells exhibited a similar LifeAct-RFP intensity profile during phagocytosis compared with control cells (Figure 3F), suggesting that beyond the significant delay in F-actin recruitment to cell-target contact sites, F-actin remodeling in phagocytosis in ninein-depleted cells remained intact.

To further confirm the defective F-actin phenotype, we used the frustrated phagocytosis assay. This extensive phagocytic atypical spreading is an active process predominantly driven by F-actin polymerization (Flannagan *et al.*, 2010; Masters *et al.*, 2013). Cells treated with ninein-targeting and nontargeting control siRNA were allowed to spread on IgG-coated coverslips for 7 min before fixing cells and immunostaining using antibodies against F-actin and ninein. Confocal imaging and immunofluorescence analysis of cell spread on the flat substrates showed that ninein-depleted cells had significantly smaller average of total F-actin-stained area compared with control cells (Figure 3, G and H), further supporting our earlier findings of defective F-actin dynamics in cells lacking ninein. Taken together, these findings suggest that ninein is critical only during early stages of membrane engagement with IgG-particles by modulating timely F-actin polymerization. Next, we utilized electron scanning microscopy (SEM) to closely examine the morphologies of individual phagocytic membranes engaging with 3.9 μm IgG-coated beads (Figure 3, I–K). In ninein-depleted cells, bound IgG-beads lacked prominent pseudopods, compared with those in control cells (Figure 3I). Thus, to quantify phagocytic cup formation and progression differences, bound beads were subdivided into three groups scored based on their surface-coverage with extending phagocytic membrane (0%, > 25–50%, > 50%; Figure 3J). Our analysis revealed that a higher percentage of bound IgG-particles in ninein-depleted cells were not associated with phagocytic membrane, compared with control cells (Figure 3, I and K). We also found that a lower percentage of IgG-beads were observed with pseudopod extensions that extended 25–50% and > 50% over the bead-surface in cells treated with ninein-targeting siRNA, compared with those

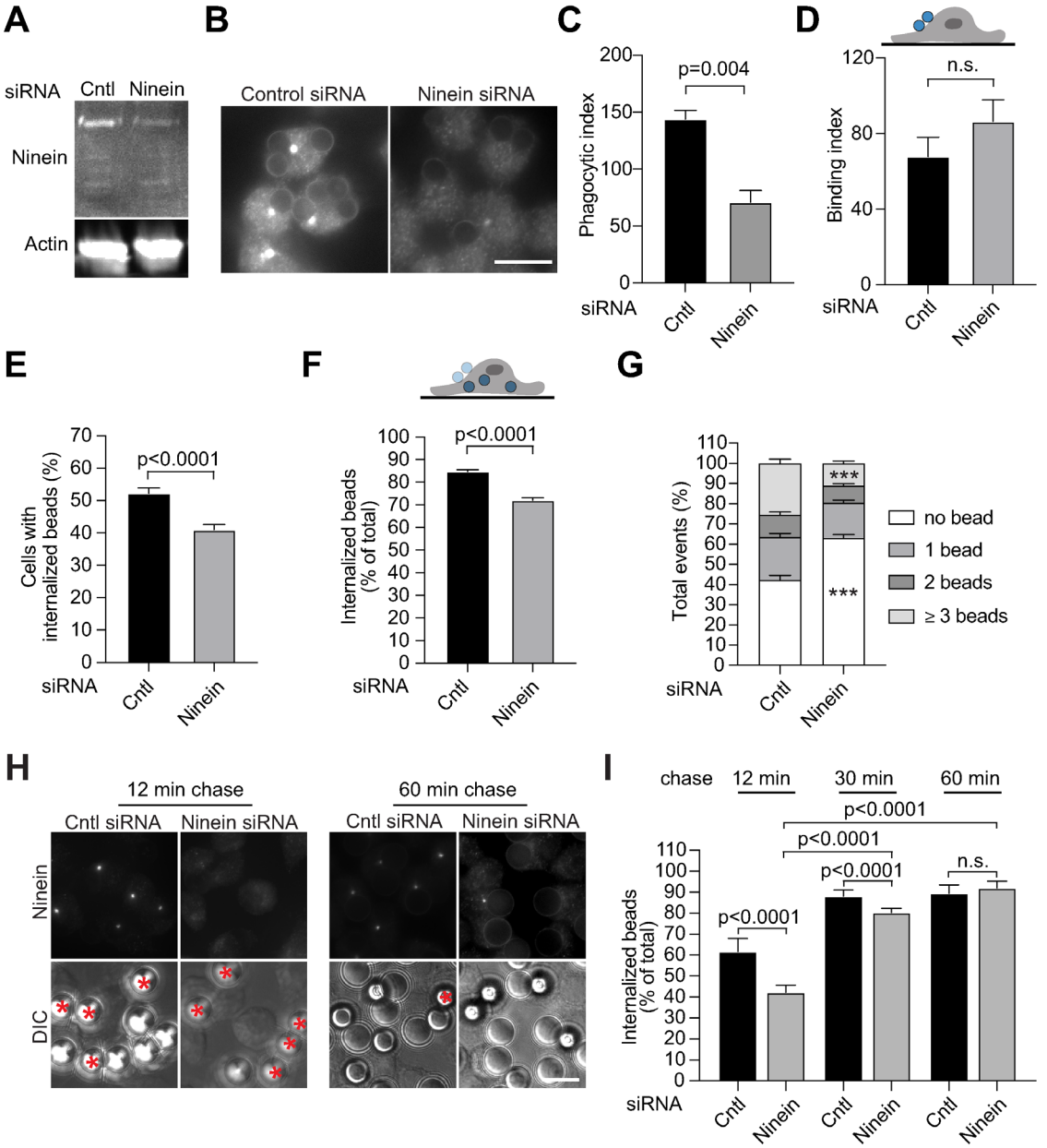

FIGURE 2: Ninein depletion in macrophages reduces phagocytosis efficiency. (A) Representative immunoblots of total cell lysates probed for ninein and β-actin in RAW cells treated with ninein-targeted SMARTpool siRNA or control siRNA. (B) Representative epifluorescence images of ninein-depleted cells and control cells challenged with 3.9-μm IgG-coated beads for a 7-min pulse, washed, and then chased for 10 min to assess phagocytosis efficiency. Cells were fixed, immunostained for bound beads and then permeabilized and immunostained for ninein. (C) Plot showing phagocytic index (the total number of beads internalized/ 100 macrophages) in cells treated with ninein-targeting or control siRNA ($n \geq 717$ cells). (D) The binding index (the total number of bound particles/ 100 macrophages) in cells treated with indicated siRNA I ($n \geq 736$ cells). (E) Quantification of the percent of RAW cells that internalized 3.9 μm IgG-beads after ninein depletion, compared with control siRNA-treated cells ($n \geq 909$ cells). Cells were exposed to IgG-beads for 7 min, washed, and incubated for a 10-min chase before fixation. Bound particles were labeled with Cy5-anti-IgG before cells were permeabilized and immunostained for ninein. (F) Percentage of internalized beads (number of beads internalized/ total bound and internalized beads) in cells treated with ninein-targeting or control siRNA ($n \geq 1687$ beads). (G) Quantification of the percentage of cells with indicated number of internalized beads. Cells treated like that in E. ($n \geq 462$ cells, *** indicate $p < 0.0001$). (H) Representative epifluorescence images of ninein-depleted cells and control cells challenged with 6.92 μm IgG-beads for 7 min, washed, and incubated for the indicated times before cells were fixed and immunostained for bound beads and then permeabilized and immunostained for ninein. Red asterisks indicate bound but not internalized particles labeled with Cy5-anti-IgG. (I) Quantification of internalized beads (number of beads internalized/ total bound and internalized beads) in cells treated with ninein-targeting or control siRNA and challenged as in (H) ($n \geq 1819$ beads). The *p*-values were calculated using two-tailed unpaired Student's *t* test (C–F) and two-way ANOVA followed by Šídák's (G) and Tukey's multiple comparisons tests (I). Data are from one experiment (G) and three independent experiments per condition (A–F, H and I). Error bars represent the standard error of the mean (C, D, and I) and standard error of proportion (E–G). Scale bar = 10 μm.

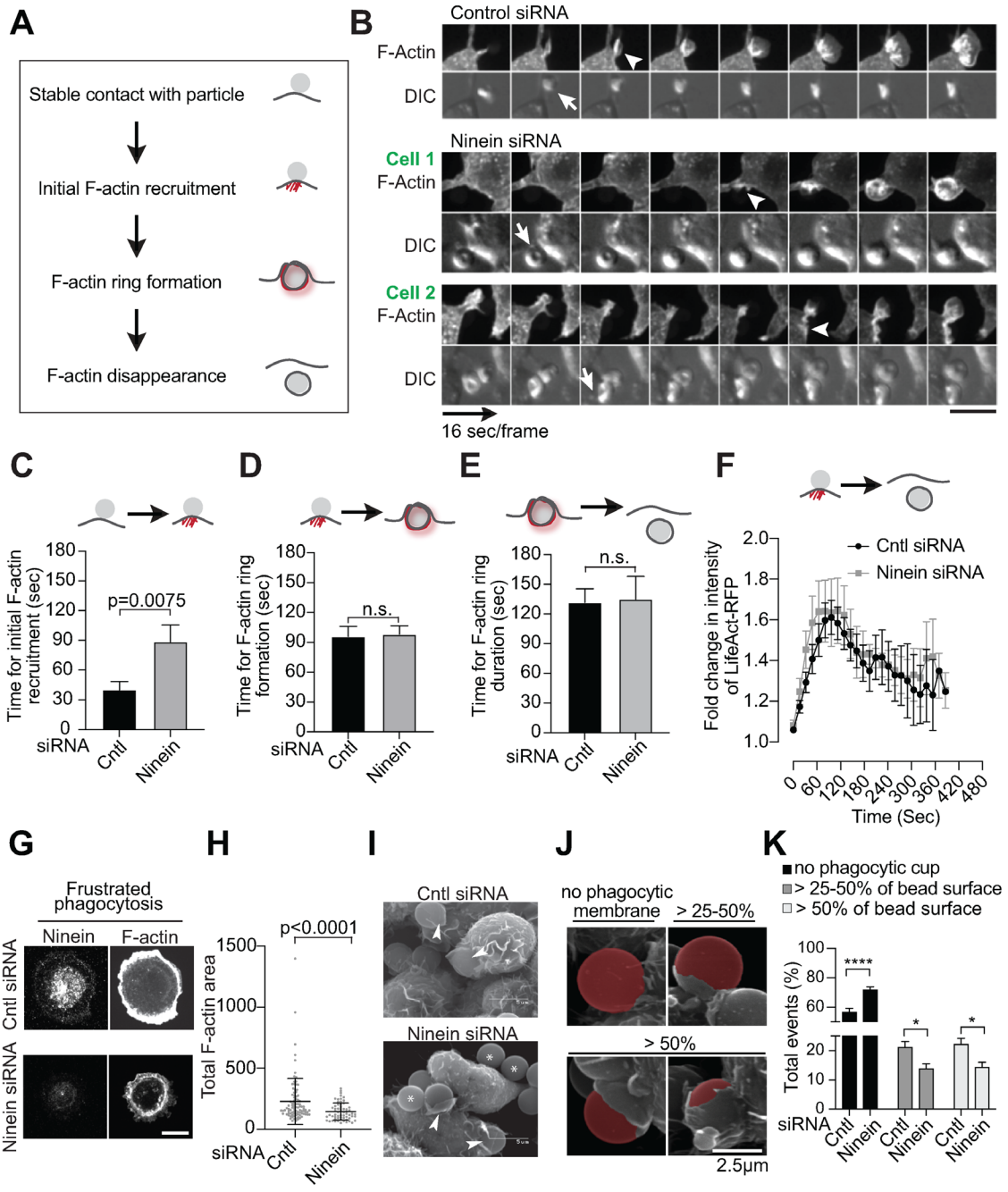

FIGURE 3: Ninein is important for F-actin recruitment and pseudopod elaboration during FcγR-mediated phagocytosis. (A) Schematic of major F-actin events following binding of IgG-sRBCs to the macrophage surface. (B) Representative confocal movie frames showing binding of IgG-sRBCs to the cell surface of RAW cells stably expressing LifeAct-RFP and treated with ninein-targeting or control siRNA. An arrow marks the binding of the IgG-particle to the macrophage surface and an arrowhead shows the initiation of F-actin polymerization. (C) Quantification of the average duration in seconds between binding of the particle to the cell surface ($t = 0$ s) and initial F-actin polymerization at the contact site ($n \geq 40$). (D) Quantification of the average duration (in seconds) between initial F-actin polymerization and the presence of a complete F-actin ring around the phagosome ($n \geq 28$). (E) Quantification of the duration between F-actin ring presence and disappearance on the phagosome ($n \geq 29$). (F) Quantification of LifeAct-RFP intensity during the entire phagocytic event using confocal live cell imaging of siRNA-treated cells. Traces showing the LifeAct-RFP signal at and around the phagosome from the initial detectable enrichment ($t = 0$ s) over time until the signal disappears from the phagosomes. Data is plotted as the ratio value of LifeAct-RFP integrated density of the phagosomes relative to the integrated density at the cell cortex using the frame just before the initial detectable enrichment ($n \geq 12$ phagocytic events per treatment). (G) Confocal images of macrophages during frustrated phagocytosis. siRNA-treated cells were allowed to spread on IgG-coated coverslips for 7 min before cells were fixed and immunostained for ninein and actin. Scale bar = 10 µm. (H) Scatterplot of spread area of RAW cells treated with indicated siRNA in (G). Dots represent total area of F-actin in single cells engaging in frustrated phagocytosis ($n \geq 62$ cells). (I) SEM micrographs of RAW cells treated

treated with control siRNA (Figure 3K), suggesting an earlier bottleneck that delayed phagocytic cup formation. However, we did not detect any structural abnormalities in phagocytic cups among ninein-depleted cells compared with control cells, as both formed tightly-associated pseudopod membranes around the circumference of the beads (arrowheads in Figure 3I). Collectively, these results suggest that the delay in F-actin recruitment in ninein-depleted cells has a direct consequence on F-actin cup initiation and timely pseudopod formation without altering phagocytic cup structure.

Delayed F-actin recruitment during phagocytosis in ninein-depleted cells is independent of PI3 kinase (PI3K) activity and IQGAP1

We next investigated potential mechanisms driving the delayed F-actin recruitment to particle attachment sites in ninein-depleted cells. An intact MT network is needed for PI3K localization and activity and pseudopod formation during FcγR-mediated phagocytosis (Khandani *et al.*, 2007). Ninein-depleted cells exhibited defects consistent with impaired PI3K recruitment and activity during pseudopod formation (Cox *et al.*, 1999; Khandani *et al.*, 2007) and during frustrated phagocytosis (Cox *et al.*, 1999), thus we monitored PI3K activity in ninein-depleted cells. PI3K activity was assessed by monitoring the phagocytic cup accumulation of the fusion protein AKT-PH-GFP, which binds to PI3K products (Ebner *et al.*, 2017). Ninein-depleted and control cells transiently transfected with the AKT-PH-GFP construct, and were then challenged with IgG-opsonized sRBCs for 4 min then immunostained for ninein. Binding of IgG-sRBCs in ninein-depleted cells induced redistribution of AKT-PH-GFP to the regions of particle uptake (Figure 4A). The analysis of the levels of AKT-PH-GFP recruited to the phagocytic cups in ninein-depleted cells was comparable to that in control cells (Figure 4B). This data indicated that ninein does not regulate PI3K recruitment during early stages of phagocytosis and indirectly implies that the MT network is likely intact at the forming cup in ninein-depleted cells.

A ninein-interactome BioID datasets in HEK293-T cells identified IQGAP1 as biotinylated with greater than sixfold enrichment relative to a BioID control (Redwine *et al.*, 2017). IQGAP1 was also implicated in F-actin cup formation and internalization of avidin-coated latex beads in RAW cells, through a direct interaction with the formin Dia1 (Brandt *et al.*, 2007). Immunostaining of RAW cells ingesting IgG-sRBCs for 4 min exhibited strong recruitment of IQGAP1 to F-actin cups, which was significantly reduced in ninein-depleted cells (Figure 4, C and D). Interestingly, depletion of IQGAP1 protein in RAW cells using ON-TARGET plus mouse IQGAP1 SMARTpool siRNA (Figure 4, E and F), did not inhibit internalization of IgG-coated latex beads compared with control cells (Figure 4G). This data suggests that ninein promotes IQGAP1 localization to the cup but the presence of IQGAP1 is not necessary for FcγR-mediated phagocytosis.

Ninein is required for particle inward movement and phagosome maturation

The mechanical process of phagosome movement toward the cell interior can take place during or after phagocytic cup closure (Vorselen *et al.*, 2020a). The mechanisms responsible for is inward movement of phagosomes is proposed to be mediated by cortical tension as the primary force (Herant *et al.*, 2011; Lee *et al.*, 2011), or forces generated by actin polymerization alone or together with myosin II contractility around the captured target (Barger *et al.*, 2020; Jaumouillé and Waterman, 2020; Vorselen *et al.*, 2021), in addition to evidence of pulling at the base of the forming phagosome (Vorselen *et al.*, 2020a, 2020b). To examine the contribution of ninein in particle internalization events, we used live cell imaging to track the uptake of IgG-sRBCs in RAW cells expressing LifeAct-RFP after treatment with ninein-targeting or nontargeting control siRNA. To overcome the observed delay in phagocytic cup formation (Figure 3) and to specifically examine the inward translocation, we tracked the position of fully or nearly formed phagosomes (assessed by an F-actin ring) in time-lapse images relative to the site of F-actin cup formation or membrane protrusion just prior the inward translocation. Importantly, we continued to track IgG particles using differential interference contrast (DIC) microscopy even after F-actin dissemination. In control cells, we discovered that during internalization, IgG-sRBCs travel for significantly longer distances intracellularly compared with cells treated with ninein-targeting siRNA (Figure 5, A–C; Supplemental Video 1), suggesting defective inward movement. Measurements of the movement of IgG-sRBCs at 5- or 8-min postinitiation of internalization showed shorter distances traveled in ninein-depleted cells compared with control cells (Figure 5C). These impaired movements suggest that the presence of ninein is needed for the early translocation during particle internalization in macrophages.

Next, we determined whether the reduced inward phagosome translocation in ninein-depleted cells was linked to delays in F-actin recruitment in the forming phagosome. We monitored F-actin recruitment from when it formed a complete ring around the target particle ($t = 0$) to when F-actin visibly dissociated from the phagosome. In ninein-depleted cells, the duration of the F-actin ring, from formation to disassembly and clearance from the phagosome, was a similar length of time, compared with that in control cells, (135.03 s ± 22.92 s vs. 131.56 s ± 13.99 s, respectively; Figure 3E). Clearance of F-actin from the base of the phagosome and accumulation at the tip, in the space between the phagosome and the plasma membrane (Scott *et al.*, 2005), is thought to coincide with internalization. Thus, we examined unilateral F-actin signal at the phagosome closure site, that coincides with the contractile activity of phagosome closure (Swanson *et al.*, 1999), target deformation (Vorselen *et al.*, 2021), and inward movement of the phagosome observed during both FcγR- and complement receptor 3 (CR3)-mediated phagocytosis (Jaumouillé *et al.*, 2019; Vorselen *et al.*, 2020b, 2021). Intensity

with ninein-targeting or control siRNA challenged with IgG-3.9 μm beads for 7 min. Arrowheads indicate particles with structurally intact phagocytic cups, where extended pseudopod structures are tightly associated with beads. Asterisks indicate particles that lacked prominent pseudopods. (J) SEM micrographs of RAW cells treated with control siRNA. IgG-beads were divided into three categories based on phagocytic membrane-coverage of beads surface. (K) Quantification of percentage of IgG-particles with indicated membrane elaborations during binding ($n \geq 389$ beads). Data are plotted as the mean from three independent experiments (B–H) and two independent experiments (I–K). The *p* values were calculated using two-tailed unpaired Student's *t* test (C–E and H) and Two-way ANOVA test followed by Šídák's multiple comparisons test (K). Error bars represent the standard error of the mean (C–F), SD (H) or the standard error of proportion (K).

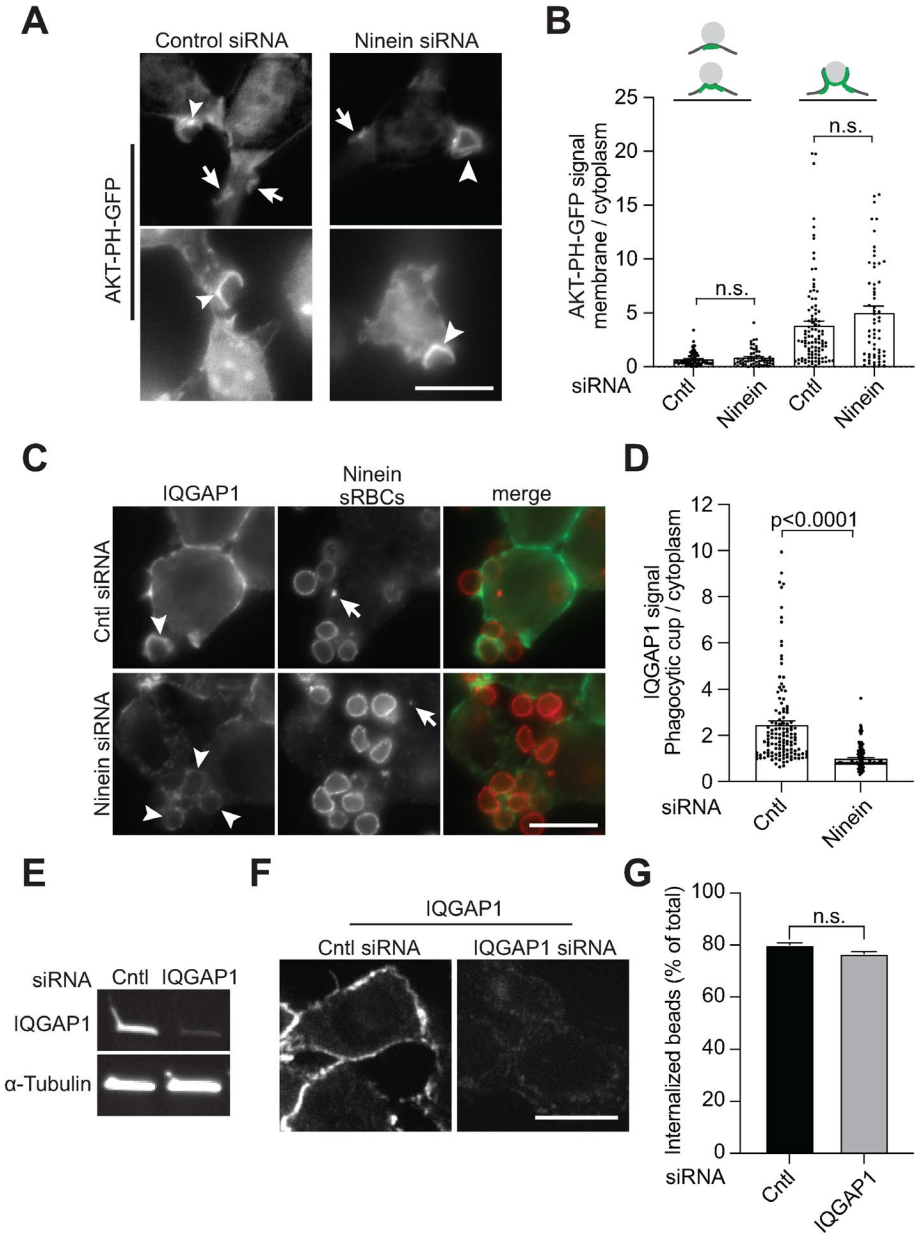

FIGURE 4: Ninein-depleted cells have normal PI3K activity but reduced IQGAP1 recruitment at phagocytic cups that does not impair internalization. (A) Representative epifluorescence images of RAW cells treated with ninein-targeting or control siRNA and transiently transfected with the AKT-PH-GFP construct and challenged with IgG-sRBCs for 4 min before fixation. Arrowhead and arrow indicate the recruitment of AKT-PH-GFP at the site of contact, and the phagocytic cup around bound particles, respectively. (B) Measurement of AKT-PH-GFP signal in RAW cells treated with indicated siRNA. Each dot represents the ratio value of integrated density at the indicated phagocytic membrane engaging with IgG-sRBCs relative to the cytoplasmic signal ($n \geq 68$). (C) Representative epifluorescence images of RAW cells treated with ninein-targeting or control siRNA that were challenged with IgG-sRBCs for 4 min before cells were fixed, immunostained for IQGAP1 and ninein. Arrowhead indicates IQGAP1 localization around bound particles, which is reduced in ninein-depleted cells. Arrow indicates ninein at the MTOC. (D) Plot of IQGAP1 signal in RAW cells treated with indicated siRNA. Each dot represents the ratio value of IQGAP1 fluorescence intensity in individual phagocytic cups engaging with IgG-sRBCs relative to the cytoplasmic signal ($n \geq 134$ event). (E) Representative immunoblots of total cell lysates of RAW cells treated with IQGAP1-targeting SMARTpool siRNA or control siRNA that were probed for IQGAP1 and anti-α-tubulin. (F) Representative confocal images of RAW cells treated with IQGAP1-targeting or control siRNA, fixed and immunostained for IQGAP1. (G) Percentage of internalized 3.9 μm beads (number of beads internalized/ total bound and internalized beads) in cells treated with IQGAP1-targeting or control siRNA ($n \geq 2375$ beads). The *p* values were calculated using two-tailed Mann-Whitney's U test (B and D) and two-tailed unpaired Student's *t* test (G). Data are plotted as the mean from three independent experiments (A, B, E, and F) and two independent experiments (C, D, and G). Error bars represent the standard error of the mean (B and D), and the standard error of proportion (G).

measurements of F-actin signal at the tip of closing phagosomes revealed similar levels of F-actin accumulation in ninein-depleted cells compared with control cells (Figure 5, D and E). Collectively, our results suggest that the defective inward phagosome translocation caused by ninein depletion is not mediated by impaired F-actin dynamics during internalization.

Next, we asked whether ninein is required during later steps of phagosome translocation toward the cell center, and maturation. Phagosomes move in cells along MT tracks centrifugally and centripetally by kinesin and dynein, respectively (Blocker *et al.*, 1997; Jordens *et al.*, 2001; Harrison and Grinstein, 2002). We tested whether ninein is required for promoting centripetal migration of phagosomes by challenging ninein-depleted cells with IgG-sRBCs and measuring phagosome speed using live cell imaging. We found that in ninein-depleted cells, more phagosomes moved toward the cell periphery whereas in control cells, the majority of phagosomes were moving toward the cell center (unpublished data). More importantly, quantification of centripetally-moving phagosomes showed reduced speeds in ninein-depleted cells, compared with control cells (Figure 5F). No significant changes in speed were observed for phagosomes moving toward the cell periphery between ninein-depleted cells, compared with control cells (Figure 5F); the movement which is potentially facilitated by kinesin (Blocker *et al.*, 1997) or Myosin-Va (Al-Haddad *et al.*, 2001). To examine the direct role for ninein activity on phagolysosome biogenesis we assessed the early onset phagosome maturation in ninein-depleted cells, compared with control cells. We induced internalization of IgG-beads for 7 min followed by washes and incubation of cells in fresh culture medium for 12-min chase. External beads were stained before cell permeabilization, and cells were immunostained for ninein and LAMP1, a lysosome and late endosome protein, marking phagosome maturation (Huynh *et al.*, 2007; Figure 5G). Indeed, we discovered that ninein-depleted cells had a significantly lower percentage of LAMP1+

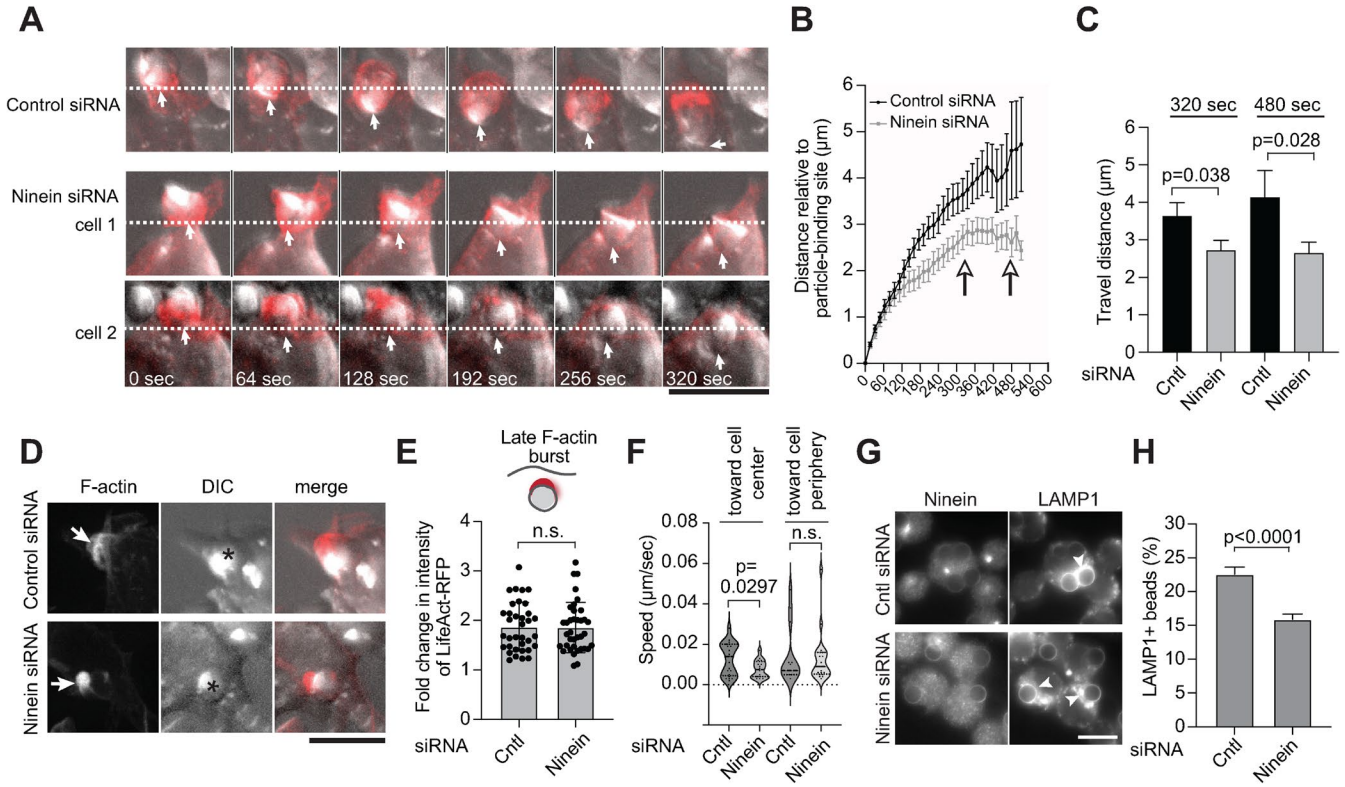

FIGURE 5: Ninein is required for the early inward particle translocation of opsonized targets. (A) Representative merges of brightfield and confocal images tracking the movement of IgG-sRBCs over 19 min in RAW cells expressing LifeAct-RFP (*red*) treated with ninein-targeting or control siRNA. Arrows indicate the position of the IgG-sRBCs over time while dashed line indicates the initial position where the particle was captured. (B) Quantification of traces showing the position of the IgG-sRBCs relative to the phagocytic cup/ membrane protrusion where inward movement was initiated (position = 0 μm) over time ($n \geq 34$ phagocytic events per treatment). Arrows indicate the time points plotted in Figure 5C. (C) Quantification of the travel distance (μm) that is defined as the distance traveled by IgG-particles relative to the phagocytic cup/ membrane protrusion where inward movement was initiated (position = 0 μm) during movies acquired with 16 s intervals ($n \geq 28$ and $n \geq 13$ events for 320 s and 480 s, respectively). (D) Representative confocal images showing F-actin polymerization concentrated at the tip of a closing phagosome in RAW cells stably expressing LifeAct-RFP and treated with ninein-targeting or control siRNA. An arrow marks the F-actin polymerization that accompanies the closure of phagocytic cups, and an asterisk shows the center of the internalizing particle. (E) Measurement of F-actin signal in RAW cells treated with indicated siRNA. Each dot represents individual measurement of the ratio value of integrated density of F-actin at the tip of the phagosome relative to the cytoplasmic signal ($n \geq 35$ events). (F) Violin plot showing the speed of individual IgG-sRBCs during retrograde ($n \geq 16$) or anterograde ($n \geq 13$) movement in 25 min movies acquired with 16 or 21 s intervals. (G) Representative epifluorescence images of RAW cells treated with ninein-targeting or control siRNA that were challenged with 3.9 μm IgG-beads for 7 min, washed and followed by a 12-min chase. Cells were fixed, immunostained for unbound particles, then permeabilized and stained for ninein and LAMP1. Arrowhead indicates LAMP1 enrichment around engulfed beads. (H) Quantification of percentage of internalized 3.9 μm IgG-beads enriched in LAMP1 in cells treated with ninein-targeting or control siRNA ($n \geq 1556$ internalized beads). The *P* values were calculated using two-tailed unpaired Student's *t* test. Error bars represent the standard error of the mean (B and C), the SD (E), and the standard error of proportion (H) from three independent experiments. Scale bars = 10 μm.

phagosomes, compared with phagosomes in control cells (Figure 5H). Collectively, our data showed that ninein depletion has significant influence on the rapid inward and long-range retrograde trafficking of phagosomes, and phagolysosome formation.

Intrigued by the presence of ninein at the phagocytic cup, we sought to test whether these enrichments facilitated the formation of noncentrosomal MTs (Supplemental Figure S1A). In polarized cells, ninein translocates from the centrosome to the cell cortex or vesicles, to stabilize noncentrosomal MT minus-ends (Mogensen *et al.*, 2000; Moss *et al.*, 2007; Goldspink *et al.*, 2017; He *et al.*, 2022). To enhance visualization of MT assemblies on the membrane we monitored MT nucleation and growth during frustrated phagocytosis. We performed 1- and 2-min MT regrowth assays in RAW cells after treatment with nocodazole (Philip *et al.*, 2022), and adherence to IgG-coated coverslips for 5–7 min. Cells were fixed and immunostained for tyrosinated-α-tubulin, to label newly formed MTs (Song and Brady, 2015). Image analysis revealed the absence of MTs at the pseudopod extensions in close contact with the coverslip (Supplemental Figure S1B). All MTs were in the radial network emanating from the MTOC. Imaging live cells transfected with GFP-EB1 also did not reveal comets emanating from sites of IgG-sRBC attachment (unpublished data). These experiments suggest that ninein does not perform known noncentrosomal MT-nucleation roles in the phagocytic cup.

The dynein complex is recruited to the phagocytic cup in a ninein-dependent manner

After establishing a requirement for ninein during early steps of phagocytosis, we hypothesized that the rapid recruitment of ninein to the phagocytic membrane may recruit and engage the dynein complex at phagocytic sites. We next examined dynein localization in macrophages and found that dynein heavy chain (HC), dynein intermediate chain 2 (IC2) and dynactin subunit p150^{Glued} all localized to the MTOC in resting cells with no visible detection at the plasma membrane (Supplemental Figure S1C). However, during phagocytosis, dynein HC, dynein IC2 and p150^{Glued} were all enriched and formed patches at the phagocytic cups within 4 min of encountering IgG-sRBCs (Figure 6A), similar to the localization of ninein (Figure 1D). Z-stack confocal slices of dynein-accumulation throughout the phagocytic cup showed that dynein was distributed at the base in addition to the sides and tips of the cups (Figure 6B). Line scan analysis of the perimeter of the phagocytic cup revealed a uniformed spatial distribution of dynein clusters around the opsonized particle (Figure 6C). Next, we examined ninein and dynein colocalization in cells seeded on IgG-coated coverslips containing noncovalently IgG-coated beads (Figure 6, D and E) to examine phagocytic events with incomplete engulfed particles (Marie-Anaïs *et al.*, 2016; Mularski *et al.*, 2018). Line scan intensity analysis revealed the accumulations of ninein with dynein HC and IC2 subunits and F-actin fluorescence signals around IgG-beads (Figure 6F). Using the colocalization threshold plugin in Fiji, we quantified the Pearson's correlation coefficients of ninein with dynein HC, dynein IC2, and F-actin (mean ± SD of 0.83 ± 0.14, 0.67 ± 0.13, and 0.64 ± 0.18; respectively; Figure 6G), showing strong colocalization of all pairs. Furthermore, measurement of the distribution of ninein with dynein HC, dynein IC2, and F-actin showed strong overlap of the pair signals around the bound particle (mean ± SD of 0.96 ± 0.06, 0.96 ± 0.08, and 0.91 ± 0.16; respectively; Figure 6H). Thus, ninein together with dynein and dynactin, form clusters around the phagocytic cup during FcγR-dependent phagocytosis.

We hypothesized that whether ninein is required as dynein cargo-adaptor then dynein and dynactin localization to phagocytic membrane should be affected by ninein depletion (Figure 7A). We examined dynein HC and p150^{Glued} localization in ninein-depleted cells that were challenged with IgG-sRBCs for 4 min. Quantification of confocal images showed that ninein-depleted cells contained a significantly lower percentage of phagocytic cups with enrichment of dynein HC and p150^{Glued} compared with control cells (Figure 7B), suggesting that ninein promoted dynein–dynactin phagocytic cup localization. Furthermore, image analysis of the persisting dynein HC and p150^{Glued} revealed that their intensity levels were significantly reduced throughout the phagocytic cup in ninein-depleted cells, compared with control cells (Figure 7, C and D, and black bars in F and G). We investigated whether extending the duration of particle contact in ninein-depleted cells would allow eventual dynein complex recruitment to the phagocytic cup. Cells were exposed to IgG-sRBCs for 4 min at 37°C, followed by wash to remove unbound IgG-sRBCs and a 14-min incubation at 4°C, a temperature that allows extended binding without particle internalization (Flannagan *et al.*, 2010). We found no significant differences in the percentages of F-actin cup formation at cold versus permissive temperatures for ninein-depleted or control cells (Figure 7E). Notably, dynein HC and P150^{Glued} were enhanced at the phagocytic cup in ninein-depleted cells after prolonged cold incubation, while control cells showed no change in dynein HC and P150^{Glued} levels (Figure 7, F and G). These results suggest potential compensatory mechanisms, possibly involving additional adaptors, when extended interactions with opsonized particles occur.

Dynein activity is critical for inward movement of bound particles during phagocytosis

Following identification of a role for ninein in the inward movement of particles and recruitment of dynein–dynactin complexes to the phagocytic cup, we next tested whether dynein activity is necessary for translocation of nascent phagosomes. To this end, we employed dynarrestin, a cell-permeable reversible dynein-binding and motility inhibitor (Höing *et al.*, 2018). First, we tested whether dynein activity was required for the engulfment of IgG-coated beads. Quantification of internalized beads relative to the total number of beads (number of internalized beads/ sum of bound and internalized beads) revealed that dynarrestin-treated cells showed a similar ability to internalize IgG-beads, compared with control cells (Figure 8A). This data suggests the presence of dynein at the cup (Figure 6) was not contributing to F-actin cup formation and pseudopod closure. Next, we investigated whether dynein activity is required for early phagosome translocation. Dynarrestin was administered for 2.5 h to LifeAct-RFP-expressing cells before they were challenged with IgG-sRBCs. In control and dynarrestin-treated cells undergoing phagocytosis, we tracked the position of IgG-particles over time (similar to Figure 5, A and B) to assess the inward movement. In control cells, IgG-sRBCs translocated intracellularly for longer distances than in cells treated with dynarrestin (Figure 8, B and C; Supplemental Video 2). Interestingly, this impaired movement in dynarrestin-treated cells was observed as early as 120 s postinitiation of the particle inward movement (Figure 8, C and D), suggesting an early role for dynein in inward translocation in phagosomes soon after/ with closure. Alternatively, the suppressed inward movement could also be a secondary effect of changes in the underlying MT cytoskeleton caused by dynarrestin treatment (Supplemental Figure S1, D and E). To examine whether the defective dynein-dependent translocation impacts phagolysosome formation, we assayed for phagosome maturation in dynarrestin-treated and control cells. Indeed, we found that dynarrestin-treated cells had a significantly lower percentage of LAMP1+ phagosomes compared with DMSO-treated control cells (Supplemental Figure S1F; Figure 8E), which further supports an early requirement of dynein-dependent motility for efficient phagosome maturation.

DISCUSSION

This study has unveiled novel and distinct roles for ninein and dynein at different stages of FcγR-mediated phagocytosis. Understood to be a centrosomal protein, we report an unexpected role for ninein at sites of bound particles where it is required to initiate F-actin recruitment and timely formation of the phagocytic cup. While particle internalization is possible in the absence of ninein, it remains slow and inefficient for particles likely due to its role in initial F-actin recruitment from mechanisms that have yet to be determined. In addition to ninein's role in F-actin recruitment at binding sites, both ninein and the motor dynein are present at the cup and contribute to an early inward movement of forming phagosomes (Figure 8F).

While less studied compared with other dynein activators (Reck-Peterson *et al.*, 2018; Olenick and Holzbaur, 2019), ninein serves as a dynein adaptor and motility activator, with emerging evidence supporting this role. Like other dynein motility activators, ninein contains N-terminal stretches of coiled-coil sequences that facilitate its association with the dynein-dynactin complex (Casenghi *et al.*, 2005; Redwine *et al.*, 2017), forming processive assemblies in vitro (Redwine *et al.*, 2017). Ninein also contains EF-hand-domains, a

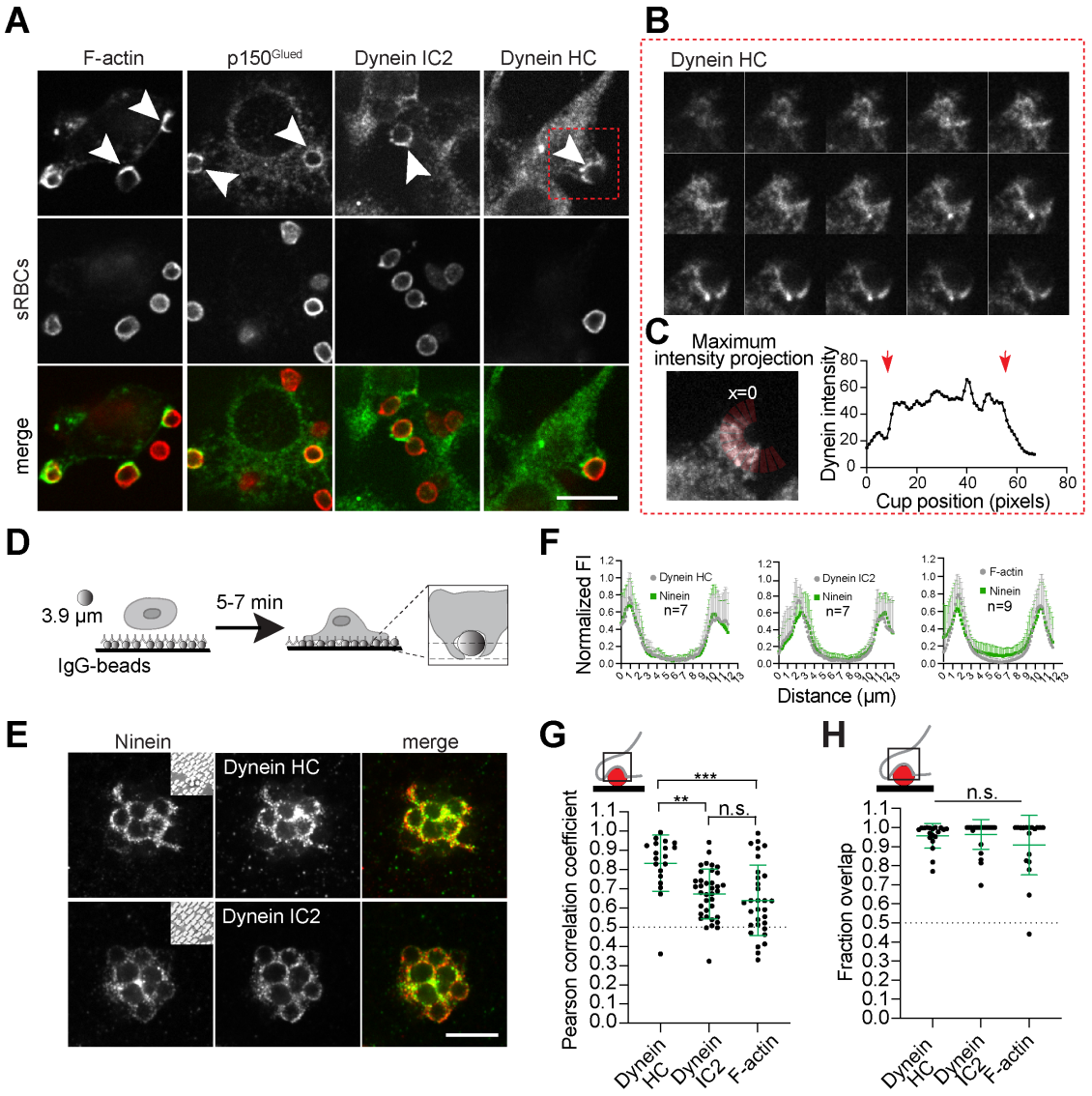

FIGURE 6: The dynein complex is recruited to the phagocytic cup. (A) Representative images of single confocal planes of RAW cells stained for dynein HC, dynein IC2, p150^{Glued}, and F-actin. Cells were stimulated for 4 min with IgG-sRBCs. Arrowheads illustrate enrichment of the indicated proteins at sites of phagocytosis before internalization. (B) Deconvolved confocal Z-series of the region indicated by the box in (A) to illustrate the distribution of dynein HC at the base and the membrane protrusions extending around the particle surface. Confocal slices are 0.3-µm apart. (C) Maximum intensity projection of full Z-stack consisting of 37 optical sections spaced 0.3-µm apart. Right panel indicates line scan profile measuring the intensities around the cup marked by the dashed line. Arrows indicate the margins of the phagocytic cup. (D) Diagram of modified frustrated phagocytosis assay (Mularski *et al.*, 2018). RAW cells were parachuted onto coverslips coated with noncovalently attached 3.9-µm IgG-beads to allow cells to form phagocytic cups around the particles without complete internalization. (E) RAW cells were allowed to spread for 7 min before being fixed and immunostained for ninein, dynein HC, dynein IC2 and F-actin (not depicted). Inset shows IgG-beads visualized by DIC. (F) Normalized intensity profile of ninein with dynein HC, dynein IC2 or F-actin signal along the phagocytic membrane around IgG-beads. (G) Plot of Pearson's correlation coefficients for the colocalization of ninein with HC, dynein IC2, and F-actin. Colocalization measurements were obtained from fluorescent signals on IgG-beads during the modified frustrated phagocytosis assays ($n \geq 19$) in Figure 5E. (H) Plot of Manders' correlation coefficients for the signal overlap of dynein HC, dynein IC2, and F-actin with ninein. Measurements were obtained from fluorescent signals on IgG-beads during the modified frustrated phagocytosis assays ($n \geq 18$) in Figure 6E. The *p* values were calculated using one-way ANOVA followed by Tukey's multiple comparisons test. Error bars represent the SD. Scale bars = 10 µm.

feature present in a subset of other dynein activators including Rab-11FIP3, Rab45, CRACR2a, and ninein-like (NINL) protein (McKenney *et al.*, 2014; Redwine *et al.*, 2017; Wang *et al.*, 2019) or adaptor-like proteins Num1 and Mcp5 in yeast (Saito *et al.*, 2006; Tang *et al.*, 2012). Notably, overexpression of ninein leads to Golgi fragmentation (Casenghi *et al.*, 2005) akin to what is observed in cells expressing mutant forms of dynein light chain, dynactin subunit p150^{Glued}, BICD2, and depletion of Lis1, NDE1 and NDEL1 (Harada *et al.*, 1998; Lam *et al.*, 2010; Neveling *et al.*, 2013; Jaarsma and Hoogenraad, 2015). Here, we show in macrophages, ninein forms distinct

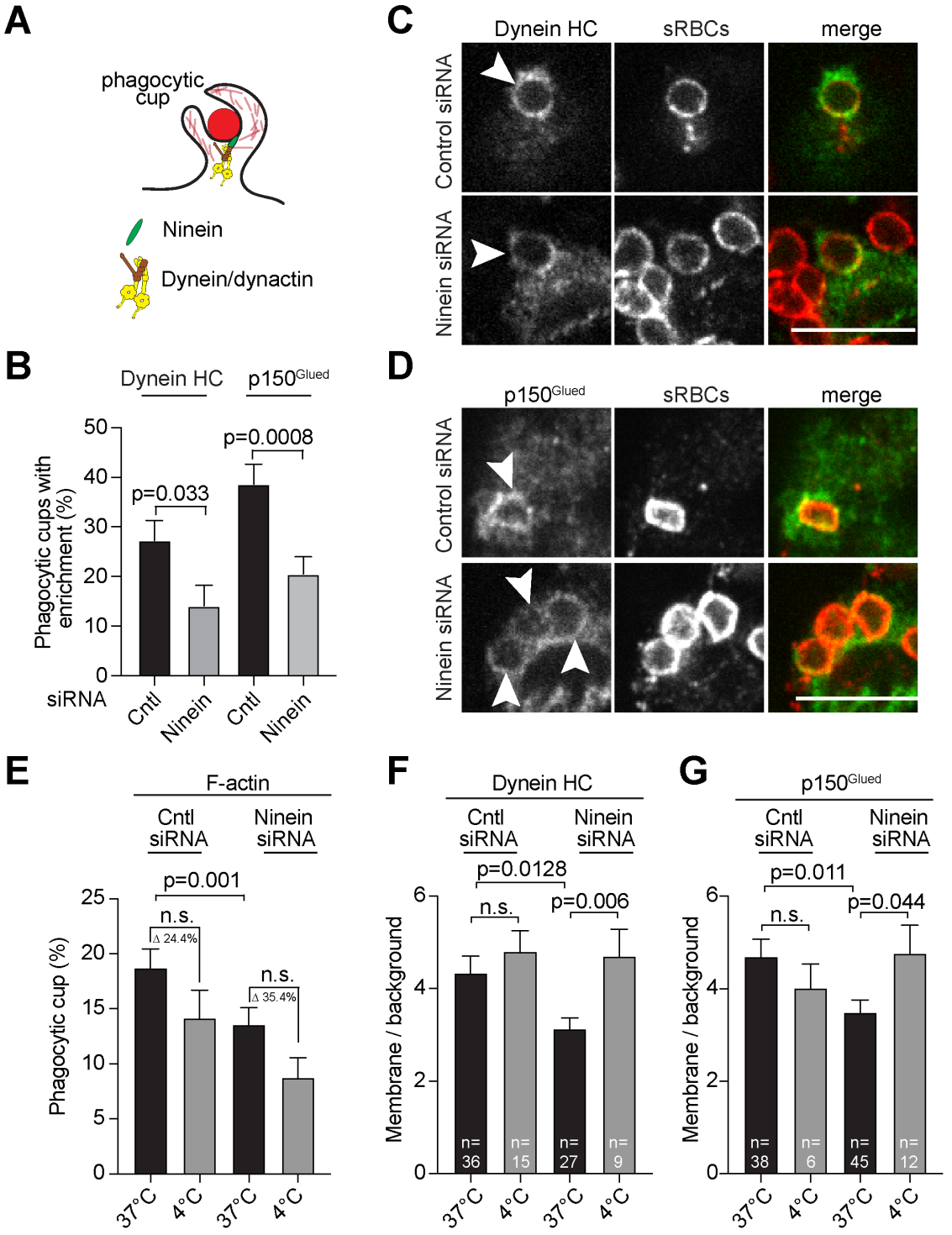

FIGURE 7: The dynein complex recruitment to the phagocytic cup requires ninein. (A) Diagram showing the recruitment of dynein and dynactin at the phagocytic cup by ninein. (B) Quantification of phagocytic cups with enrichment of dynein ($n \geq 71$) or dynactin subunit p150^{Glued} ($n \geq 141$) in RAW cells treated with ninein-targeting or control siRNA and then challenged with IgG-sRBCs for 4 min. (C and D) Representative confocal images of single confocal slices of RAW cells stained for dynein HC, and p150^{Glued}. Ninein-depleted and control cells were stimulated for 4 min with IgG-sRBCs. Arrowheads illustrate the localization of the indicated proteins at sites of phagocytosis before internalization. (E) RAW cells treated with ninein-targeting or control siRNA then challenged with IgG-sRBCs at 37°C for 4 min (black bars), washed, and further incubated at 4°C for additional 14 min (grey bars) to inhibit internalization. Cells were fixed and immunostained to visualize ninein and actin ($n \geq 184$). (F and G) Plot of the phagocytic cup localization of dynein HC and dynactin subunit p150^{Glued} at 37 or 4°C depicted as ratio value of integrated density at the phagocytic cup relative to background signal. Cells were treated similar to E, immunostained to visualize ninein and dynein HC or dynactin subunit p150^{Glued}. *p* values were calculated using two-tailed unpaired Student's *t* test from two independent experiments (B) and from three independent experiments (C-E). Error bars represent the standard error of proportion (B and E) and the standard error of the mean (F and G). Scale bars = 10 μm.

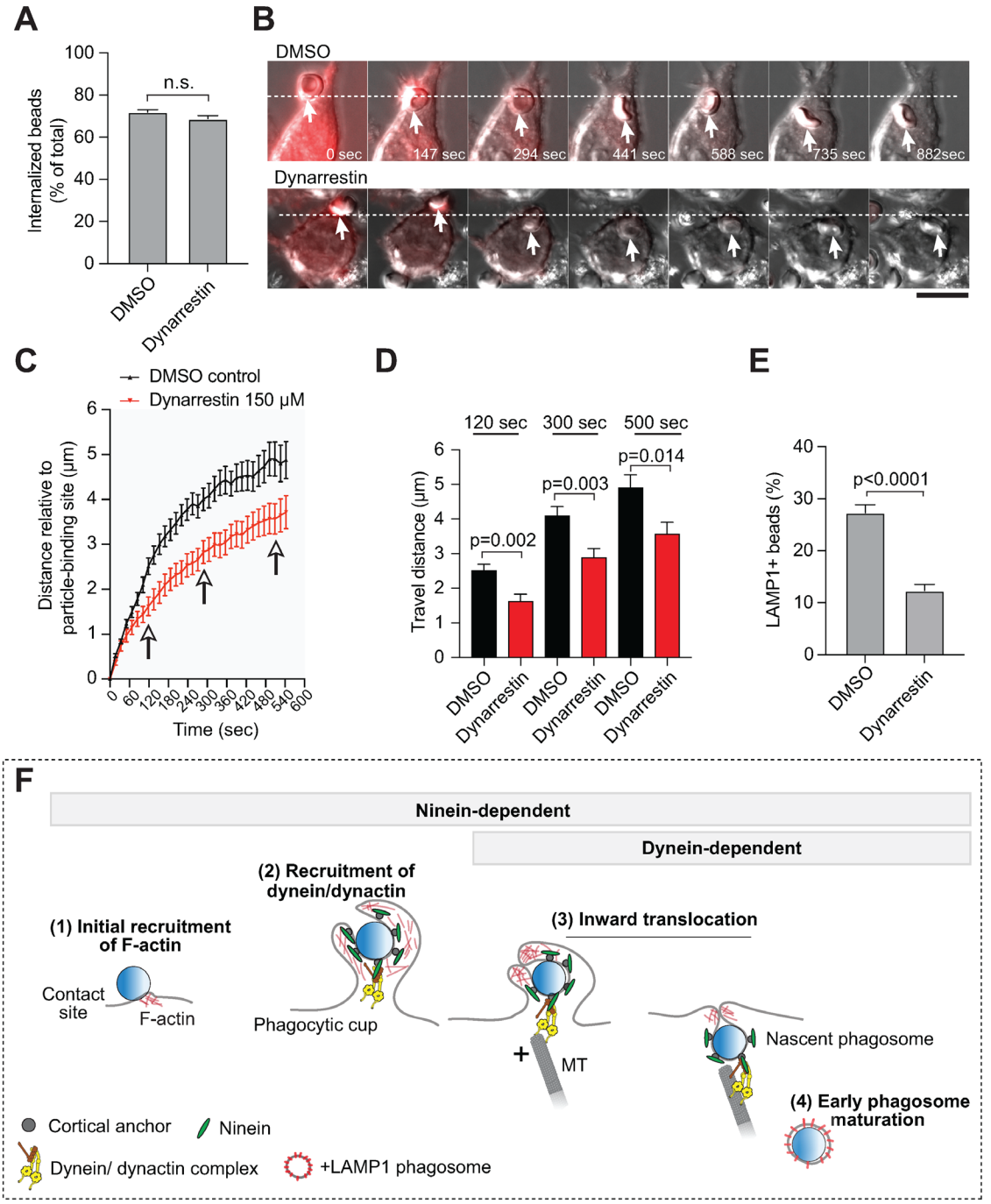

FIGURE 8: Dynein motility is required for the early inward movement of phagosomes. (A) Percentage of internalized 3.9-µm beads (number of beads internalized/ total bound and internalized beads) in cells treated with DMSO or 150 µM dynarrestin for 2.5 h ($n \geq 927$ beads). (B) Representative merge of DIC and epifluorescence images showing the movement of IgG-sRBCs that were tracked for about 25 min during internalization in RAW cells expressing LifeAct-RFP (*red*) treated with DMSO or 150 µM dynarrestin for 2.5 h. Arrows indicate the position of the IgG-sRBCs over time while dashed line indicates the position where the particle was captured. (C) Quantification of traces showing the position of the IgG-sRBCs relative to the phagocytic cup/ membrane protrusion where inward movement was initiated (position = 0 µm) over time. RAW cells expressing LifeAct-RFP were treated with 150 µM dynarrestin or DMSO for 2.5 h before being challenged with IgG-sRBCs and imaged for 25 min at 17 s intervals (n ≥ 24 phagocytic events per treatment). (D) Quantification of the travel distance of IgG-particles at indicated time points during internalization (n ≥ 24). (E) Quantification of the percentage of LAMP1+ phagosomes containing 3.9 µm IgG-beads in cells treated with 150 µM dynarrestin or DMSO for 2.5 h ($n \geq 723$ internalized beads). The *p* values were calculated using two-tailed unpaired Student's *t* test. Error bars represent the standard error of proportion (A and E) and the standard error of mean (C and D) from three independent experiments. (F) Model depicting the role of ninein in phagocytosis. After binding, ninein is required for initial F-actin recruitment at the particle contact site to promote timely cup formation and efficient internalization. Ninein enhances dynein-dynactin complex recruitment to the phagocytic cup. The presence of ninein and the activity of dynein are important for the early inward translocation and efficient phagosome formation, likely through interactions with the MT cytoskeleton.

puncta that decorate the phagocytic cup and colocalize with dynein and dynactin within minutes of macrophage engagement with IgG-coated target particles. Dynamic recruitment of dynein-dynactin to plasma membrane patches oc0curs at the leading edge of migrating cells (Levy and Holzbaur, 2008), on the cortex of activated T cells to facilitate MTOC reorientation (Combs *et al.*, 2006; Yi *et al.*, 2013; Wang *et al.*, 2019), and at the yeast cell cortex to drive spindle repositioning (Lee *et al.*, 2003; Xiang and Fischer, 2004). During these events, dynein interacts with MT plus-ends to drag the MTOC/ nuclei/ spindles closer to the cell cortex. While we have shown that MTOC reorientation also occurs during FcγR-mediated phagocytosis (Eng *et al.*, 2007), this event occurs postinternalization and thus does not likely involve the early dynein-mediated activity identified here.

Dynein is well-known to associate with early and late phagosomes (Blocker *et al.*, 1997; Habermann *et al.*, 2001; Rai *et al.*, 2016), and mediate MT minus-end intracellular trafficking and phagosome maturation (Harrison and Grinstein, 2002; Harrison *et al.*, 2003). However, the precise mechanisms underlying dynein recruitment to the phagosome membrane and the timing of this process have remained unclear. Here, we provide evidence that ninein and dynein complex recruitment during phagocytosis are spatially and temporally coordinated. Ninein recruits and colocalizes with dynein–dynactin puncta on the forming phagocytic cup and likely contribute to the initial inward translocation of the nascent phagosome. Dynamic MTs ends penetrate phagocytic sites during CR3- (Lewkowicz *et al.*, 2008), and FcγR-mediated phagocytosis (Binker *et al.*, 2007; Khandani *et al.*, 2007). Our observed early requirement for dynein activity for nascent phagosome translocation likely contributes to MT minus-end directed trafficking of phagosomes and efficient acquisition of lysosomal proteins and maturation into a phagolysosome compartment. Membrane-associated dynein clusters have been shown to capture MT plus-ends to initiate dynein minus-end motility (Combs *et al.*, 2006; Omer *et al.*, 2018; Wang *et al.*, 2019), supporting this theory. Similar clusters of dynein–dynactin facilitate higher collective forces on late phagosomes (Rai *et al.*, 2016). There is likely a suite of dynein adaptors that participate along with ninein to mediate dynein recruitment for phagosome movement. Lis1, a dynein motility activator, is found at the phagocytic cup and is required for FcγR-mediated phagocytosis (Chhatre *et al.*, 2020). Both ninein and Lis1 may be simultaneously engaged with dynein as ninein binds to the tail of dynein, similar to other cargo-adaptors (Reck-Peterson *et al.*, 2018) together with dynactin (Urnavicius *et al.*, 2015), while Lis1 binds to the motor domain to relieve dynein auto-inhibition (Qiu *et al.*, 2019; Marzo *et al.*, 2020; Gillies *et al.*, 2022). The dynein adaptor RILP, a Rab7 binding protein, is also well-known to play a critical role in dynein recruitment to promote phagosome movement and phagolysosome formation (Harrison *et al.*, 2003). A heterogenous population of dynein cargo-adaptors is thus likely recruited to the surface of the phagosome, either directly from the cytosol or by fusion with endosomal vesicles. Additional factors such as cholesterol participate in forming specialized microdomains on the phagosome membrane (Dermine *et al.*, 2005; Rai *et al.*, 2016), where dynein is associated for phagosome trafficking (Rai *et al.*, 2016).

How ninein regulates the local initial F-actin polymerization at the cell cortex after particle binding is not clear. Because the subsequent F-actin remodeling during phagocytic cup and phagosome formation are otherwise normal, this suggests that ninein mediates early signaling events following FcγR ligation. We previously showed that intact MTs are required for PIK activity during FcγR-mediated phagocytosis (Khandani *et al.*, 2007). The upstream signaling elements Src and Syk lead to the recruitment of the lipid kinase PI3K to generate modified lipids that recruit a variety of actin regulators, leading to activation of the Arp2/3 actin nucleator (Fitzer-Attas *et al.*, 2000; Gu *et al.*, 2003; Jaumouillé and Grinstein, 2016). Because we observed normal AKT-PH-GFP accumulation at particle binding sites in ninein-depleted cells, this implies that these upstream signaling elements are intact and active in the absence of ninein.

We also examined recruitment of molecules downstream of PI3K activity during phagocytosis in ninein-depleted cells. PI3K is a positive regulator of Rac1 and Cdc42 (Campa *et al.*, 2015) which activate Arp2/3 complex at the phagocytic cup (Cox *et al.*, 1997; Dart *et al.*, 2012). Rac1 and Cdc42 bind IQGAP1 (Hart *et al.*, 1996; Kuroda *et al.*, 1996) in polarized kidney cells to facilitate MT plus-end capture via CLIP-170 (Goldspink *et al.*, 2017). Interestingly, ninein knockdown significantly reduced accumulation of IQGAP1 in the phagocytic cup. IQGAP1 and Rac1 are critical during cell migration to recruit the actin nucleator Dia1 to form the actin meshwork driving the leading edge (Watanabe *et al.*, 2004; Brandt and Grosse, 2007). Additionally, CLIP-170 can directly recruit Dia1 to the phagocytic cup (Lewkowicz *et al.*, 2008). These dynamic and complex interactions between the MT and actin cytoskeletal networks speak to their important interplay to drive major morphological changes at the plasma membrane. There are further complexities in membrane protrusions that capture target particles, depending on the phagocytic receptor engaged. For instance, while we observed that IQGAP1 knockdown does not impact uptake of IgG-opsonized particles, it does significantly reduce internalization of avidin-coated latex beads (Brandt *et al.*, 2007). Similarly, Dia1 is required for CR3-mediated phagocytosis (Colucci-Guyon *et al.*, 2005), which employs membrane ruffles for particle capture (Patel and Harrison, 2008), but Dia1 is dispensable for FcγR-mediated phagocytosis (Colucci-Guyon *et al.*, 2005). In addition to IQGAP1, a ninein BioID interactome in HEK293-T cells showed interactions with other actin regulators including cortactin (Redwine *et al.*, 2017). Cortactin binds, stabilizes and activates Arp2/3 complexes in vitro (Weaver *et al.*, 2001), and localizes to the leading edge in migrating cells (Daly, 2004). Our future work will employ BioID proximity labeling to resolve nineinbinding partners at the phagocytic cup to mechanistically understand ninein's contributions during phagocytosis in macrophages. In summary, we identify a novel noncentrosomal role for ninein in promoting F-actin recruitment, timely phagocytic cup formation and particle internalization. Additionally, we show that cortical ninein recruits dynein and dynactin to mediate inward particle translocation important for subsequent phagosome maturation.

MATERIALS AND METHODS

Request a protocol through *Bio-protocol*.

Antibodies and reagents

Cells were immunostained with the following primary antibodies: mouse anti-α-tubulin (1:10000; T9026, MilliporeSigma, Canada Co., Oakville, ON), mouse anti-ninein (1:500, sc-376420, Santa Cruz Biotechnology, Santa Cruz, CA), rabbit anti-ninein (1:300, ABN1720; MilliporeSigma), mouse anti-pan actin (1:200, AAN02, Cytoskeleton, Denver, CO), mouse anti-dynein HC (1:100, sc-514579, Santa Cruz Biotechnology), mouse anti-dynein IC2 (1:500, sc-13524, Santa Cruz Biotechnology), mouse anti-dynein p150^{Glued} (1:500, 610474, BD Biosciences, Mississauga, ON), mouse anti-LAMP1 (1:100, sc-19992, Santa Cruz Biotechnology), human IgG (I4506, MilliporeSigma.), mouse anti β-actin (1:1000, A5441, MilliporeSigma.), mouse anti-IQGAP1 (1:300, sc-374307, Santa Cruz Biotechnology)

and DAPI (1:10000, MilliporeSigma.). Cy3, Cy2, and Cy5 donkey antirat, antimouse, antihuman and antirabbit secondary antibodies (diluted 1:500) were purchased from Jackson ImmunoResearch Laboratories (West Grove, PA). Sheep red blood cells (sRBCs) were obtained from MP Biomedical (ICN55876, Solon, OH). Rabbit anti-sRBC IgG (ICN55806) was obtained from MP Biomedical. The 3.87 µm (PS05003) and 6.92 µm (PS06004) crosslinked polystyrene divinylbenzene beads were purchased from Bangs Laboratories (Fishers, IN). Plasmid expressing human EB1-GFP (JB131) was a gift from Tim Mitchison & Jennifer Tirnauer (Addgene plasmid # 39299). Plasmid expressing AKT-PH-GFP was a gift from Dr. Sergio Grinstein. DAKO Fluorescence mounting media was purchased from Agilent Technologies Canada (Mississauga, ON). DMEM, fetal bovine serum (FBS), and phosphate-buffered saline (PBS) were purchased from Wisent (St-Bruno, QC). ON-TARGET plus mouse ninein SMARTpool siRNA (L-062136-01-0010), and ON-TARGET plus mouse IQGAP1 SMARTpool siRNA (L-040589-01-0005), and ON-TARGET plus nontargeting pool siRNA (D-001810-10-05) were purchased from Dharmacon (Lafayette, CO). Dynarrestin was purchased from Tocris Bioscience (6526, Toronto, ON).

Cell culture and siRNA transfection

The RAW 264.7 (RAW) murine macrophage cell line was purchased from the American Type Culture Collection (ATCC; Manassas, VA). RAW cells between passages four and 22 were cultured and maintained in complete DMEM containing 10% heat-inactivated FBS at 37°C in a 5% CO_2. To deplete ninein and IQGAP1, 0.5×10^5 or 0.2×10^6 cells were seeded into coverslips on 24-well plate or six-well plate, respectively, for ~24 h before addition of the ninein-targeting or control siRNA for 48 h with a daily dosing of 50 or 100 nM siRNA. Transfection of siRNA was done with Lipofectamine 3000 Transfection Reagent (L3000001, Thermo Fisher Scientific, Waltham, MA) according to the manufacturer's instruction. LifeAct-RFP (Riedl *et al.*, 2008) was transfected into RAW cells using Lipofectamine 3000 and clones were chemically selected over several weeks followed by cell sorting to enrich for low to medium expressers by Dr. He Song Sun For live imaging 0.2×10^6 LifeAct-RFP cells were plated overnight into 35-mm glass-bottom single well dishes (P35G-1.5-14-C, MatTek, Ashland, MA). Cells were transfected with ninein-targeting or control siRNA using Lipofectamine 3000 Transfection Reagent for 48 h with a daily dosing of 50 nM siRNA.

Imaging

For indirect immunofluorescence, cells were cultured on glass coverslips and fixed with ice-cold methanol at -20°C for 10 min or in 4% paraformaldehyde for 20 min and permeabilized with 0.1% TritonX-100 in PBS containing 100 mM glycine for 20 min. Cells were blocked and antibodies were diluted in PBS containing 3% bovine serum albumin (BSA; BioShop Canada, Ontario) and 1% FBS. Epifluorescence images were acquired using a Zeiss AxioObserver Z1 inverted epifluorescence microscope with a 63 × 1.4 NA oil immersion lens (Carl Zeiss Canada, Toronto, ON) equipped with an Axiocam 506 mono-camera (Carl Zeiss Canada, Toronto, ON) and configured using Zeiss Zen 3.1 software for image capture. Confocal images were acquired on a Quorum WaveFX-X1 spinning disk confocal microscope (Quorum Technologies, Guelph, ON) configured with MetaMorph image acquisition software (Molecular Devices LLC, Sunnyvale, CA) with a 63x oil immersion objective equipped with a cooled electron-multiplying charged-coupled device (EM-CCD) camera (Hamamatsu) housed in the Center of Neurobiology of Stress, University of Toronto. Cells were kept at 37°C and 5% CO_2 throughout live cell imaging.

Phagocytosis assays

IgG-opsonization of polystyrene beads and sRBCs. IgG-opsonization was performed by incubating a prewashed 100–200 µl of 10% suspension sRBCs with 2 µg/ml antisheep IgG in PBS. IgG opsonization using 3.9 and 6.9 µm beads was performed by washing the beads with PBS and opsonizing with 2 mg/ml human IgG at 1:1 ratio in PBS. Both targets (sRBCs and beads) were incubated for 1 h on a rotator at room temperature. Unbound IgG was washed off, and IgG-sRBCs and IgG-beads were resuspended in PBS.

Binding assays. IgG-coated targets were added to RAW cells for 4 min (for IgG-sRBCs) and 7 min (for 3.9 and 6.9 µm IgG-beads) that are of different densities to descend and initiate binding to the RAW cell surface and induce phagocytic cup formation without complete internalization at 37°C and 5% CO_2. Challenged cells were washed with PBS to remove unbound particles. Cells were then fixed with ice-cold methanol for 10 min in -20°C, stained with a Cy3, Cy2, or Cy5 conjugated secondary antibody against the opsonizing IgG antibody. Binding index was tabulated as normalized number of particles bound per 100 macrophages relative to the control.

Internalization and phagosome maturation assays. IgG-coated 3.9 and 6.92 µm latex beads were incubated with pretreated RAW cells (for the specific times see Figure Legends) at 37°C and 5% CO_2. Wells were then washed twice with prewarmed media to remove unbound beads before cells were further incubated with fresh medium for 10, 12, 30, and 60 min. Incubations exceeding 12 min were performed in siRNA-containing medium. Cells were washed with PBS to remove medium and fixed with 4% PFA in PBS for 20 min. To label bound but not internalized beads, cells were incubated with Cy5 conjugated secondary antibody that was diluted in PBS to label unbound IgG-beads for 10 min then washed with PBS before cell permeabilization with 0.1% TritonX-100 in PBS containing 100 mM glycine for another 20 min. Internalization index was tabulated as the percent of internalized beads divided by the sum of bound and internalized beads. To quantify LAMP1-enriched phagosomes, a unified threshold was applied to the epifluorescence images in Fiji version 2.9.0 (National Institutes of Health, Bethesda, MD), and particles above the threshold intensities were defined. Enriched phagosomes were tabulated as the percent of the internalized beads with enhanced LAMP1 signal divided by the sum of internalized beads.

Frustrated phagocytosis. RAW cells were grown on six-well tissue culture plates to 40–60% confluency before they were detached by mechanical scraping. Coverslips on 12-well or 24-well plates were incubated with subagglutinating concentrations of human IgG in PBS for 1 h on a rotator at room temperature. Unbound IgG were washed off using PBS. Cells were added in complete medium or in medium containing the indicated siRNA treatment (Figure 3, G and H) and were allowed to spread for 7 min at 37°C. Cells were fixed with ice-cold methanol at -20°C for 10 min and immunostained for the indicated proteins. To quantify frustrated phagocytosis spreading, cells were stained for ninein and F-actin. In Fiji, the cell boundaries postfrustrated phagocytosis were measured using maximum intensity projections of F-actin confocal slices. A unified threshold was applied followed by using the Analyze Particles tool in Fiji with the minimum particle size set at 50 pixels.

Frustrated phagocytosis with noncovalently attached opsonized particles. Coverslips on 12-well or six-well plates were incubated with subagglutinating concentrations of human IgG in PBS for

30 min at room temperature with shaking. Polystyrene 3.9 μm beads and sRBCs were incubated using similar antibodies concentrations as listed above of human IgG antibody and rabbit anti-sRBC IgG, respectively for 30 min at room temperature with shaking. Opsonized-particles were then added to opsonized coverslips and incubated for 30 min at room temperature with shaking. Excessive IgG and unbound particles were washed off before RAW cells were added and incubated for 5–7 min before fixation with ice-cold methanol at -20°C for 10 min. To plot the intensity profile of ninein, dynein HC, dynein IC2, and actin along the particle perimeter, we used the line tool in Fiji to draw a line across the particle and used Plot Profile tool to graph the intensity along the line. To measure colocalization and co-occurrence of ninein with dynein HC, dynein IC2, and actin, we used the Colocalization threshold plugin in Fiji. Pearson's correlation coefficients and Manders' overlap correlation coefficients were calculated for individual beads in two-color confocal images.

Live cell imaging of phagocytosis. On 35 mm glass-bottom single well dishes, treated LifeAct-RFP stably expressing RAW cells (with siRNA or drugs) were mounted on Quorum WaveFX-X1 spinning disk confocal microscope or Zeiss AxioObserver Z1 inverted epifluorescence microscope. Cells were imaged with a 63 × 1.4 NA oil immersion lens at 37°C and 5% CO_2 throughout imaging. IgG-sRBCs were added while the RAW cells were on the microscope stage. Time lapse images were captured over a 25-min period at 16 or 21 s intervals. We used the mTrack plugin in Fiji to track the internalization distance of opsonized particles by tracking the position of the particle using DIC imaging relative to the site of an F-actin cup or membrane pseudopods.

F-actin dynamics during particle binding and uptake was assessed as described in (Naik *et al.*, 2020). Using live cell confocal imaging of LifeAct-RFP-transfected cells treated with ninein-targeting or control siRNA, we scored for the different stages of F-actin dynamics during phagocytosis. To avoid including passive events where IgG-sRBCs non-specifically attach to the surface of RAW cells, F-actin dynamics were only measured for particles that were eventually successfully internalized. Initial F-actin recruitment was measured from the time when IgG-sRBCs formed firm, nonoscillating contact with the cell surface to the first unambiguous sign of F-actin local presence on the cell surface in close vicinity to the attached particle. The initiation of F-actin recruitment usually coincided with local membrane protrusions or pseudopods around the target particle. Phagocytic events at the periphery of macrophages (vs. the dorsal surface) were chosen to examine F-actin cup and pseudopod elaboration. The duration of F-actin ring formation was calculated as the time between the initial F-actin presence at the particle contact site to a complete ring formation of F-actin around the particle. F-actin ring duration was calculated as the time from ring formation to F-actin dissociation from the phagosome. The late F-actin burst was defined as the unilateral F-actin polymerization forming postcup formation that localized in the space between the phagosome and the plasma membrane. Fold change in LifeAct-RFP intensity for single time point analysis, was obtained by measuring actin signal around the phagosome. Measurements were then normalized relative to the cytoplasmic signal for each individual phagosome. To quantify F-actin intensity, we used the fluorescence intensity selection tool within Fiji. This involved selecting a region encompassing the internalized particle from maximum intensity projection of confocal frames of optical sections spaced 0.4 μm apart that were acquired at 16 s intervals. Initial F-actin recruitment ($t = 0$) represent the time of detectable F-actin presence on the cell surface to the attached particle. For each phagocytic event, measurement was carried out until F-actin dissociates from the phagosome. Change in intensity for each phagocytic event was normalized relative to the signal at the phagocytic site before particle binding for each individual trace.

To examine noncentrosomal MTs in live movies, 0.2×10^6 LifeAct-RFP RAW cells were plated into 35-mm glass-bottom single well dishes and transfected the next day with EB1-GFP plasmid (1.5 or 2 μg DNA) with FuGENE HD Transfection Reagent (E2311, Promega, Indianapolis, IN) and used within 24 h of plasmid transfection. IgG-sRBCs were added while the RAW cells were on the microscope stage. Each Z-stack consisted of 21 optical sections spaced 0.4 μm apart that were acquired at 21 s intervals.

Transient transfection of AKT-PH-GFP was performed using Lipofectamine 3000 Transfection Reagent. 0.75 μg of AKT-PH-GFP was transfected for 24 h before challenging cells with IgG-sRBCs. The accumulation of AKT-PH-GFP at the phagosome cup was measured from epifluorescence images using the selection tool in Fiji. Measurements were obtained as a ratio of the integrated density of AKT-PH-GFP signal at the phagosome cup relative to the value of the cytoplasm.

Dynein inhibition assays. Dynein inhibition in RAW cells was performed using dynarrestin, a reversible cytoplasmic dynein 1 and 2 inhibitor (Höing *et al.*, 2018). 0.5×10^5 RAW cells or 0.2×10^6 LifeAct-RFP RAW cells were cultured onto coverslips on 24-well plates or 35-mm glass-bottom single well dishes, respectively overnight before addition of 150 μM dynarrestin in DMSO, or DMSO alone, for 2.5 h before the phagocytic assays. Live-cell imaging of dynarrestin-treated cells was conducted using an inverted epifluorescence microscope with a 63x oil immersion objective. Fluorescence and DIC images were acquired over a 25-min period at 16.8-18 s intervals. Live imaging was acquired within 5 h of treatment of dynarrestin. To track inward movement, we used mTrack plugin in Fiji to measure the internalization distance of opsonized particles by tracking the position of the particle relative to the site of formation of F-actin-rich phagocytic cup or membrane protrusion. MT total integrated fluorescence was measured in maximum intensity projection images by using the free selection tool in Fiji to encompass the cell and background area. The total MT fluorescence were measured as Integrated Density minus the (area of selected cell multiplied by mean fluorescence of background readings).

MT regrowth assays were performed by depolymerizing the MT network by treating RAW cells in suspension with culture medium containing 10 μM nocodazole for 20 min at room temperature while rotating. Cells were then cultured on coverslips coated with human IgG for 5–7 min before the cells were washed extensively with PBS to remove nocodazole, then incubated with pre–warmed culture medium to induce MT nucleation at 37°C and 5% CO_2. Cells were fixed in methanol at -20°C for 10 min after 1 or 2 min of MT regrowth. Cells were immunostained with anti-tyrosinated-α-tubulin and with Cy5-antihuman secondary antibodies. Each Z-stack consisted of 49 optical sections spaced 0.3-μm apart. The tight adherence of the cells to the IgG-coated coverslip resulted in imaging contrast on the Cy5-immunostained coverslip which was used to indicate the outlines of the frustrated membrane.

Scanning electron microscopy (SEM)

0.5×10^5 RAW cells were seeded onto coverslips in 24-well plates for 24 h before addition of 100 nM of the indicated siRNA. Cells were then challenged with IgG-opsonized 3.9 μm beads for 7 min at 37°C and 5% CO_2. Cells were washed twice with PBS and fixed with 2% glutaraldehyde for 1 h at room temperature and stored at 4°C

overnight. Cells where then washed with 0.1 M sodium cacodylate buffer, and were post fixed with 1% OsO_4 for 1 h, then washed consecutively with 1% tannic acid for 1 h, 1% OsO_4 for 30 min, and 4% uric acid for 30 min in the dark, then dehydrated using a series of ethanol washes from 70 to 100%. The samples were then critical-point dried using a Leica CPD300 (Leica Camera, Germany) and mounted onto aluminum stubs and coated with OsO_4 using an osmium plasma coater (Filgen, Japan). Images were acquired on a Hitachi S530 SEM (20kV) using Quartz PCI software. The selection tool in Fiji software was used to estimate the area covered by the phagocytic membrane by drawing a circle corresponding to 3.9 µm beads that was overlaid onto membrane protrusions in contact with the particle.

Immunoblotting

For immunoblotting, ninein targeted or control siRNA were lysed on ice with ice-cold RIPA lysis buffer (10 mM Tris-HCl, 150 mM NaCl, 1% Triton X-100, 0.1% SDS, 1 mM ethylenediaminetetraacetic acid, pH 7.4) supplemented with protease inhibitor cocktail (P8340, MilliporeSigma.) and Laemmli sample buffer (161-0737, BioRad Laboratories, Hercules, CA). Cell lysates were boiled for 10 min and then lysates were separated on 4–20% Mini-PROTEAN TGX (4561096, BioRad) and transferred to nitrocellulose membranes for 60–90 mins. Nitrocellulose membranes were then blocked for 1 h in Tris-buffered saline with 0.1% Tween® 20 detergent with 5% BSA and probed with rabbit anti-ninein (1:300), mouse anti-β-actin (1:1000), mouse anti-IQGAP1 (1:300), and mouse anti-α-tubulin (1:1000) overnight at 4°C. Goat horseradish peroxidase (HRP)-conjugated antimouse (115-035-146, Jackson ImmunoResearch Laboratories) or goat HRP-conjugated anti-rabbit (711-035-152, Jackson ImmunoResearch Laboratories) were used at 1:10,000 dilutions. Chemiluminescence signals were acquired and imaged using a ChemiDoc Imaging System (Bio-Rad). Immunoblots were exposed for durations ranging from 0.3–4 s without saturating the camera's pixels.

Statistical methods

Statistical significance was determined using two-tailed unpaired Student's *t* test, one-way and two-way ANOVA followed by Tukey's or Šídák's multiple comparisons test. Statistical analyses were conducted using Graphpad Prism V9 (GraphPad Software, La Jolla, CA), with $p < 0.05$ considered statistically significant.Abbreviations used:

ACKNOWLEDGMENTS

S.O. is a recipient of a University of Toronto Provosts Postdoctoral Award and a Canadian Institutes of Health Research (CIHR)-REDI award (ED6-190720). R.E.H. is supported by a grant from CIHR (PJT-166084). SEM stubs were prepared by Durga Acharya. Imaging work is supported by a Canada Foundation for Innovation grant (#493864) that was used to establish the Centre for the Neurobiology of Stress at UTSC.

REFERENCES

Al-Haddad A, Shonn MA, Redlich B, Blocker A, Burkhardt JK, Yu H, Hammer JA 3rd, Weiss DG, Steffen W, Griffiths G, Kuznetsov SA (2001). Myosin Va bound to phagosomes binds to F-actin and delays microtubule-dependent motility. Mol Biol Cell 12, 2742–2755..

Araki N, Hatae T, Furukawa A, Swanson JA (2003). Phosphoinositide-3-kinase-independent contractile activities associated with Fcγ-receptor-mediated phagocytosis and macropinocytosis in macrophages. J Cell Sci 116, 247–257.

Baird DH, Myers KA, Mogensen M, Moss D, Baas PW (2004). Distribution of the microtubule-related protein ninein in developing neurons. Neuropharmacology 47, 677–683.

Barger SR, Reilly NS, Shutova MS, Li O, Maiuri P, Heddleston JM, Mooseker MS, Flavell RA, Svitkina T, Oakes PW, *et al.* (2019). Membrane-cytoskeletal crosstalk mediated by myosin-I regulates adhesion turnover during phagocytosis. Nat Commun 10, 1249.

Barger SR, Gauthier NC, Krendel M (2020). Squeezing in a Meal: Myosin functions in phagocytosis. Trends Cell Biol 30, 157–167.

Binker MG, Zhao DY, Pang SJY, Harrison RE (2007). Cytoplasmic linker Protein-170 enhances spreading and phagocytosis in activated macrophages by stabilizing microtubules. J Immunol 179, 3780–3791.

Blocker A, Severin FF, Burkhardt JK, Bingham JB, Yu H, Olivo J-C, Schroer TA, Hyman AA, Griffiths G (1997). Molecular requirements for bi-directional movement of phagosomes along microtubules. J Cell Biol 137, 113–129.

Bouckson-Castaing V, Moudjou M, Ferguson DJP, Mucklow S, Belkaid Y, Milon G, Crocker PR (1996). Molecular characterisation of ninein, a new coiled-coil protein of the centrosome. J Cell Sci 13, 179–190.

Brandt DT, Grosse R (2007). Get to grips: Steering local actin dynamics with IQGAPs. EMBO Rep 8, 1019–1023.

Brandt DT, Marion S, Griffiths G, Watanabe T, Kaibuchi K, Grosse R (2007). Dia1 and IQGAP1 interact in cell migration and phagocytic cup formation. J Cell Biol 178, 193–200.

Campa CC, Ciraolo E, Ghigo A, Germena G, Hirsch E (2015). Crossroads of PI3K and Rac pathways. Small GTPases 6, 71–80.

Campellone KG, Welch MD (2010). A nucleator arms race: Cellular control of actin assembly. Nat Rev Mol Cell Biol 11, 237–251.

Casenghi M, Barr FA, Nigg EA (2005). Phosphorylation of Nlp by Plk1 negatively regulates its dynein-dynactin-dependent targeting to the centrosome. J Cell Sci 118, 5101–5108.

Castellano F, Chavrier P, Caron E (2001). Actin dynamics during phagocytosis. Semin Immunol 13, 347–355.

Chen C-H, Howng S-L, Cheng T-S, Chou M-H, Huang C-Y, Hong Y-R (2003). Molecular characterization of human ninein protein: two distinct subdomains required for centrosomal targeting and regulating signals in cell cycle. Biochem Biophys Res Commun 308, 975–983.

Chhatre A, Sanghavi P, Mallik R (2020). Lis1 co-localizes with actin in the phagocytic cup and regulates phagocytosis. Cytoskeleton 77, 249–260.

Colucci-Guyon E, Niedergang F, Wallar BJ, Peng J, Alberts AS, Chavrier P (2005). A role for mammalian diaphanous-related formins in complement receptor (CR3)-mediated phagocytosis in macrophages. Curr Biol 15, 2007–2012.

Combs J, Kim SJ, Tan S, Ligon LA, Holzbaur ELF, Kuhn J, Poenie M (2006). Recruitment of dynein to the Jurkat immunological synapse. Proc Natl Acad Sci USA 103, 14883–14888.

Cox D, Chang P, Zhang Q, Reddy PG, Bokoch GM, Greenberg S (1997). Requirements for both Rac1 and Cdc42 in membrane ruffling and phagocytosis in Leukocytes. J Exp Med 186, 1487–1494.

Cox D, Tseng C-C, Bjekic G, Greenberg S (1999). A Requirement for phosphatidylinositol 3-Kinase in pseudopod extension. J Biol Chem 274, 1240–1247.

Daly RJ (2004). Cortactin signalling and dynamic actin networks. Biochem J 382, 13–25.

Dart AE, Donnelly SK, Holden DW, Way M, Caron E (2012). Nck and Cdc42 co-operate to recruit N-WASP to promote FcγR-mediated phagocytosis. J Cell Sci 125, 2825–2830.

Delgehyr N, Sillibourne J, Bornens M (2005). Microtubule nucleation and anchoring at the centrosome are independent processes linked by ninein function. J Cell Sci 118, 1565–1575.

Dermine JF, Goyette G, Houde M, Turco SJ, Desjardins M (2005). Leishmania donovani lipophosphoglycan disrupts phagosome microdomains in J774 macrophages. Cell Microbiol 7, 1263–1270.

Ebner M, Lučić I, Leonard TA, Yudushkin I (2017). PI(3,4,5)P3 engagement restricts Akt activity to cellular membranes. Mol Cell 65, 416–431.e6.

Eng EW, Bettio A, Ibrahim J, Harrison RE (2007). MTOC reorientation occurs during FcR-mediated phagocytosis in macrophages. Mol Biol Cell 18, 2389–2399.

Fitzer-Attas CJ, Lowry M, Crowley MT, Finn AJ, Meng F, Defranco AL, Lowell CA (2000). Fcgamma Receptor-mediated phagocytosis in macrophages lacking the Src family tyrosine kinases Hck, Fgr, and Lyn. J Exp Med 191, 669–682.

Flannagan RS, Harrison RE, Yip CM, Jaqaman K, Grinstein S (2010). Dynamic macrophage "probing" is required for the efficient capture of phagocytic targets. J Cell Biol 191, 1205–1218.

Gillies JP, Reimer JM, Karasmanis EP, Lahiri I, Htet ZM, Leschziner AE, Reck-Peterson SL (2022). structural basis for cytoplasmic Dynein-1 regulation by Lis1. eLife 11, e71229.

Goldspink DA, Rookyard C, Tyrrell BJ, Gadsby J, Perkins J, Lund EK, Galjart N, Thomas P, Wileman T, Mogensen MM (2017). Ninein is essential for apico-basal microtubule formation and CLIP-170 facilitates

its redeployment to non-centrosomal microtubule organizing centres. Open Biol 7, 160274.
Gu H, Botelho RJ, Yu M, Grinstein S, Neel BG (2003). Critical role for scaffolding adapter Gab2 in FcγR-mediated phagocytosis. J Cell Biol 161, 1151–1161.
Habermann A, Schroer TA, Griffiths G, Burkhardt JK (2001). Immunolocalization of cytoplasmic dynein and dynactin subunits in cultured macrophages: enrichment on early endocytic organelles. J Cell Sci 114, 229–240.
Harada A, Takei Y, Kanai Y, Tanaka Y, Nonaka S, Hirokawa N (1998). Golgi vesiculation and lysosome dispersion in cells lacking cytoplasmic dynein. J Cell Biol 141, 51–59.
Harrison RE, Bucci C, Vieira OV, Schroer TA, Grinstein S (2003). Phagosomes fuse with late endosomes and/or lysosomes by extension of membrane protrusions along microtubules: Role of Rab7 and RILP. Mol Cell Biol 23, 6494–6506.
Harrison RE, Grinstein S (2002). Phagocytosis and the microtubule cytoskeleton. Biochem Cell Biol 80, 509–515.
Hart MJ, Callow MG, Souza B, Polakis P (1996). IQGAP1, a calmodulin-binding protein with a rasGAP-related domain, is a potential effector for cdc42Hs. EMBO Journal 15, 2997–3005.
He L, van Beem L, Snel B, Hoogenraad CC, Harterink M (2022). PTRN-1 (CAMSAP) and NOCA-2 (NINEIN) are required for microtubule polarity in Caenorhabditis elegans dendrites. PLoS Biol 20, e3001855.
Herant M, Lee CY, Dembo M, Heinrich V (2011). Protrusive push versus enveloping embrace: Computational model of phagocytosis predicts key regulatory role of cytoskeletal membrane anchors. PLoS Comput Biol 7, e1001068.
Höing S, Yeh T-Y, Baumann M, Martinez NE, Habenberger P, Kremer L, Drexler HCA, Küchler P, Reinhardt P, Choidas A, *et al*. (2018). Dynarrestin, a novel inhibitor of cytoplasmic dynein. Cell Chem Biol 25, 357–369.e6.
Huynh KK, Eskelinen EL, Scott CC, Malevanets A, Saftig P, Grinstein S (2007). LAMP proteins are required for fusion of lysosomes with phagosomes. EMBO Journal 26, 313–324.
Jaarsma D, Hoogenraad CC (2015). Cytoplasmic dynein and its regulatory proteins in Golgi pathology in nervous system disorders. Front Neurosci 9, 397.
Jaumouillé V, Cartagena-Rivera AX, Waterman CM (2019). Coupling of β2 integrins to actin by a mechanosensitive molecular clutch drives complement receptor-mediated phagocytosis. Nat Cell Biol 21, 1357–1369.
Jaumouillé V, Grinstein S (2016). Molecular mechanisms of phagosome formation. Microbiol Spectr 4, https://doi.org/10.1128/microbiolspec.MCHD-0013-2015.
Jaumouillé V, Waterman CM (2020). Physical constraints and forces involved in phagocytosis. Front Immunol 11, 1097.
Jordens I, Fernandez-Borja M, Marsman M, Dusseljee S, Janssen L, Calafat J, Janssen H, Wubbolts R, Neefjes J.(2001). The Rab7 effector protein RILP controls lysosomal transport by inducing the recruitment of dynein-dynactin motors. Curr Biol 11, 1680–1685.
Khandani A, Eng E, Jongstra-Bilen J, Schreiber AD, Douda D, Samavarchi-Tehrani P, Harrison RE (2007). Microtubules regulate PI-3K activity and recruitment to the phagocytic cup during Fcγ receptor-mediated phagocytosis in nonelicited macrophages. J Leukoc Biol 82, 417–428.
Kovari DT, Wei W, Chang P, Toro JS, Beach RF, Chambers D, Porter K, Koo D, Curtis JE (2016). Frustrated phagocytic spreading of J774A-1 macrophages ends in Myosin II-dependent contraction. Biophys J 111, 2698–2710.
Kuroda S, Fukata M, Kobayashi K, Nakafuku M, Nomura N, Iwamatsu A, Kaibuchi K (1996). Identification of IQGAP as a putative target for the small GTPases, Cdc42 and Rac1. J Biol Chem 271, 23363–23367.
Lam C, Vergnolle MAS, Thorpe L, Woodman PG, Allan VJ (2010). Functional interplay between LIS1, NDE1 and NDEL1 in dynein-dependent organelle positioning. J Cell Sci 123, 202–212.
Lecland N, Hsu CY, Chemin C, Merdes A, Bierkamp C (2019). Epidermal development requires ninein for spindle orientation and cortical microtubule organization. Life Sci Alliance 2, e201900373.
Lee CY, Herant M, Heinrich V (2011). Target-specific mechanics of phagocytosis: Protrusive neutrophil response to zymosan differs from the uptake of antibody-tagged pathogens. J Cell Sci 124, 1106–1114.
Lee WL, Oberle JR, Cooper JA (2003). The role of the lissencephaly protein Pac1 during nuclear migration in budding yeast. J Cell Biol 160, 355–364.
Levin R, Grinstein S, Canton J (2016). The life cycle of phagosomes: formation, maturation, and resolution. Immunol Rev 273, 156–179.
Levin R, Grinstein S, Schlam D (2015). Phosphoinositides in phagocytosis and macropinocytosis. Biochim Biophys Acta Mol Cell Biol Lipids 1851, 805–823.
Levy JR, Holzbaur ELF (2008). Dynein drives nuclear rotation during forward progression of motile fibroblasts. J Cell Sci 121, 3187–3195.
Lewkowicz E, Herit F, Clainche CL, Bourdoncle P, Perez F, Niedergang F (2008). The microtubule-binding protein CLIP-170 coordinates mDia1 and actin reorganization during CR3-mediated phagocytosis. J Cell Biol 183, 1287–1298.
Lin C-C, Cheng T-S, Hsu C-M, Wu C-H, Chang L-S, Shen Z-S, Yeh H-M, Chang L-K, Howng S-L, Hong Y-R (2006). Characterization and functional aspects of human ninein isoforms that regulated by centrosomal targeting signals and evidence for docking sites to direct gamma-tubulin. Cell Cycle 5, 2517–2527.
Marie-Anaïs F, Mazzolini J, Herit F, Niedergang F (2016). Dynamin-actin cross talk contributes to phagosome formation and closure. Traffic 17, 487–499.
Martín-Cófreces NB, Robles-Valero J, Cabrero JR, Mittelbrunn M, Gordón-Alonso M, Sung CH, Alarcón B, Vázquez J, Sánchez-Madrid F (2008). MTOC translocation modulates IS formation and controls sustained T cell signaling. J Cell Biol 182, 951–962.
Marzo MG, Griswold JM, Markus SM (2020). Pac1/LIS1 stabilizes an uninhibited conformation of dynein to coordinate its localization and activity. Nat Cell Biol 22, 559–569.
Masters TA, Pontes B, Viasnoff V, Li Y, Gauthier NC (2013). Plasma membrane tension orchestrates membrane trafficking, cytoskeletal remodeling, and biochemical signaling during phagocytosis. Proc Natl Acad Sci USA 110, 11875–11880.
McKenney RJ, Huynh W, Tanenbaum ME, Bhabha G, Vale RD (2014). Activation of cytoplasmic dynein motility by dynactin-cargo adapter complexes. Science 345(1979), 337–341.
Mogensen MM, Malik A, Piel M, Bouckson-Castaing V, Bornens M (2000). Microtubule minus-end anchorage at centrosomal and non-centrosomal sites: the role of ninein. J Cell Sci 113, 3013–3023.
Moss DK, Bellett G, Carter JM, Liovic M, Keynton J, Prescott AR, Lane EB, Mogensen MM (2007). Ninein is released from the centrosome and moves bi-directionally along microtubules. J Cell Sci 120, 3064–3074.
Mularski A, Marie-Anaïs F, Mazzolini J, Niedergang F (2018). Observing Frustrated Phagocytosis and Phagosome Formation and Closure Using Total Internal Reflection Fluorescence Microscopy (TIRFM). In: Macrophages: Methods and Protocols, ed. G Rousselet, New York, NY: Springer New York, 165–175.
Naik U, Nguyen QPH, Harrison RE (2020). Binding and uptake of single and dual-opsonized targets by macrophages. J Cell Biochem 121, 183–199.
Neveling K, Martinez-Carrera LA, Hölker I, Heister A, Verrips A, Hosseini-Barkooie SM, Gilissen C, Vermeer S, Pennings M, Meijer R, *et al*. (2013). Mutations in BICD2, which encodes a golgin and important motor adaptor, cause congenital autosomal-dominant spinal muscular atrophy. Am J Hum Genet 92, 946–954.
Ohama Y, Hayashi K (2009). Relocalization of a microtubule-anchoring protein, ninein, from the centrosome to dendrites during differentiation of mouse neurons. Histochem Cell Biol 132, 515–524.
Olenick MA, Holzbaur EL (2019). Dynein activators and adaptors at a glance. J Cell Sci 132, jcs227132.
Omer S, Greenberg SR, Lee W-L (2018). Cortical dynein pulling mechanism is regulated by differentially targeted attachment molecule Num1. eLife 7, e36745.
Patel PC, Harrison RE (2008). Membrane ruffles capture C3bi-opsonized particles in activated macrophages. Mol Biol Cell 19, 4628–4639.
Philip R, Fiorino C, Harrison RE (2022). Terminally differentiated osteoclasts organize centrosomes into large clusters for microtubule nucleation and bone resorption. Mol Biol Cell 33, ar68.
Piel M, Meyer P, Khodjakov A, Rieder CL, Bornens M (2000). The respective contributions of the mother and daughter centrioles to centrosome activity and behavior in vertebrate cells. J Cell Biol 7, 317–330.
Qiu R, Zhang J, Xiang X (2019). LIS1 regulates cargo-adapter-mediated activation of dynein by overcoming its autoinhibition in vivo. J Cell Biol 218, 3630–3646.
Rai A, Pathak D, Thakur S, Singh S, Dubey AK, Mallik R (2016). Dynein clusters into lipid microdomains on phagosomes to drive rapid transport toward lysosomes. Cell 164, 722–734.
Reck-Peterson SL, Redwine WB, Vale RD, Carter AP (2018). The cytoplasmic dynein transport machinery and its many cargoes. Nat Rev Mol Cell Biol 19, 382–398.

Redwine WB, DeSantis ME, Hollyer I, Htet ZM, Tran PT, Swanson SK, Florens L, Washburn MP, Reck-Peterson SL (2017). The human cytoplasmic dynein interactome reveals novel activators of motility. eLife 6, e28257.
Riedl J, Crevenna AH, Kessenbrock K, Yu JH, Neukirchen D, Bista M, Bradke F, Jenne D, Holak TA, Werb Z, *et al.* (2008). Lifeact: A versatile marker to visualize F-actin. Nat Methods 5, 605–607.
Rougerie P, Miskolci V, Cox D (2013). Generation of membrane structures during phagocytosis and chemotaxis of macrophages: Role and regulation of the actin cytoskeleton. Immunol Rev 256, 222–239.
Saito TT, Okuzaki D, Nojima H (2006). Mcp5, a meiotic cell cortex protein, is required for nuclear movement mediated by dynein and microtubules in fission yeast. J Cell Biol 173, 27–33.
Schroer TA (2004). Dynactin. Annu Rev Cell Dev Biol 20, 759–779.
Scott CC, Dobson W, Botelho RJ, Coady-Osberg N, Chavrier P, Knecht DA, Heath C, Stahl P, Grinstein S (2005). Phosphatidylinositol-4, 5-bisphosphate hydrolysis directs actin remodeling during phagocytosis. J Cell Biol 169, 139–149.
Song Y, Brady ST (2015). Post-translational modifications of tubulin: Pathways to functional diversity of microtubules. Trends Cell Biol 25, 125–136.
Swanson JA, Johnson MT, Beningo K, Post P, Mooseker M, Araki N (1999). A contractile activity that closes phagosomes in macrophages. J Cell Sci 112, 307–316.
Tang X, St Germain B, Lee WL (2012). A novel patch assembly domain in Num1 mediates dynein anchoring at the cortex during spindle positioning. J Cell Biol 196, 743–756.
Urnavicius L, Zhang K, Diamant AG, Motz C, Schlager MA, Yu M, Patel NA, Robinson CV, Carter AP (2015). The structure of the dynactin complex and its interaction with dynein. Science (1979) 347, 1441–1446.
Vorselen D, Barger SR, Wang Y, Cai W, Theriot JA, Gauthier NC, Krendel M (2021). Phagocytic "teeth" and myosin-II "jaw" power target constriction during phagocytosis. eLife, e68627.
Vorselen D, Labitigan RLD, Theriot JA (2020a). A mechanical perspective on phagocytic cup formation. Curr Opin Cell Biol 66, 112–122.
Vorselen D, Wang Y, de Jesus MM, Shah PK, Footer MJ, Huse M, Cai W, Theriot JA (2020b). Microparticle traction force microscopy reveals subcellular force exertion patterns in immune cell–target interactions. Nat Commun 11.
Wang Y, Huynh W, Skokan TD, Lu W, Weiss A, Vale RD (2019). CRACR2a is a calcium-activated dynein adaptor protein that regulates endocytic traffic. J Cell Biol 218, 1619–1633.
Watanabe T, Wang S, Noritake J, Sato K, Fukata M, Takefuji M, Nakagawa M, Izumi N, Akiyama T, Kaibuchi K (2004). Interaction with IQGAP1 links APC to Rac1, Cdc42, and actin filaments during cell polarization and migration. Dev Cell 7, 871–883.
Waterman-storer CM, Karki SB, Kuznetsov SA, Tabb JS, Weiss DG, Langford GM, F Holzbaur EL (1997). The interaction between cytoplasmic dynein and dynactin is required for fast axonal transport. Proc Natl Acad Sci USA 94, 12180–12185.
Weaver AM, Karginov AV, Kinley AW, Weed SA, Li Y, Parsons JT, Cooper JA (2001). Cortactin promotes and stabilizes Arp2/3-induced actin filament network formation. Curr Biol 11, 370–374.
Xiang X, Fischer R (2004). Nuclear migration and positioning in filamentous fungi. Fungal Genet Biol 41, 411–419.
Yi J, Wu X, Chung AH, Chen JK, Kapoor TM, Hammer JA (2013). Centrosome repositioning in T cells is biphasic and driven by microtubule end-on capture-shrinkage. J Cell Biol 202, 779–792.